Title

Photogrammetric Analysis of the 2013 El Reno Tornado Combined with Mobile X-Band Polarimetric Radar Data

Journal

Monthly Weather Review, 143(7)

ISSN

0027-0644

Authors

Wakimoto, Roger M
Atkins, Nolan T
Butler, Kelly M
et al.

Publication Date

2015-07-01

DOI

10.1175/mwr-d-15-0034.1

Peer reviewed

Photogrammetric Analysis of the 2013 El Reno Tornado Combined with Mobile X-Band Polarimetric Radar Data

ROGER M. WAKIMOTO

Department of Atmospheric and Oceanic Science, University of Colorado, Boulder, Colorado

NOLAN T. ATKINS AND KELLY M. BUTLER*

Department of Atmospheric Sciences, Lyndon State College, Lyndonville, Vermont

HOWARD B. BLUESTEIN, KYLE THIEM, JEFFREY SNYDER,+ AND JANA HOUSER#

School of Meteorology, University of Oklahoma, Norman, Oklahoma

(Manuscript received 19 January 2015, in final form 13 March 2015)

ABSTRACT

This study presents rapid-scanning X-band polarimetric radar data combined with photogrammetry of the El Reno tornado of 31 May 2013. The relationship between the hook echo, weak-echo hole (WEH), weak-echo column (WEC), and the rotational couplet with the visual characteristics of the tornado are shown. For the first time, cross-correlation coefficient (ρ_{hv}) and differential reflectivity (Z_{DR}) data are included in the photogrammetric analyses. The tornado was accompanied by a large tornadic debris signature (TDS) with a diameter ~2 km wide during the analysis time. The center of the TDS was not collocated with the WEH and the rotational couplet. Instead, the TDS was displaced ~1 km to the north and within the weak-echo notch of the hook echo. A ''debris overhang'' was identified in vertical cross sections of the ρ_{hv} fields. The overhang was located in a weak-echo trench and a notch of high ρ_{hv}, consistent with the position of the tornado updraft. The updraft was hypothesized to be carrying small debris particles to heights that produced the overhang signature. A U-shaped band of high ρ_{hv} and Z_{DR} was resolved in a vertical cross section and positioned at the periphery of the WEC during one of the analysis times. It was proposed that the band formed as a result of hydrometeors encircling the WEC while being surrounded on all sides by relatively hydrometeor-free air. The characteristics of the scatterers within the WEC were resolved and believed to be composed of a low concentration of very small, randomly oriented, debris particles, even in the presence of strong centrifuging, and a general absence of hydrometeors.

1. Introduction

One of the most important achievements in recent years is the high-resolution documentation of the kinematic structure of the hook echo and intense circulations accompanying the tornado that has resulted from the deployment of mobile Doppler radars near severe storms (e.g., Bluestein et al. 1993, 1997, 2004, 2007a,b; Wurman et al. 1996; Wurman and Gill 2000; Alexander and Wurman 2005; Wurman et al. 2007a,b; Wurman and Kosiba 2013). These measurements have revealed the detailed structure of the tornadic vortex signature (TVS; Brown et al. 1978) and the weak-echo hole (WEH) that frequently develop within the hook echo (e.g., Fujita 1981; Wakimoto et al. 1996; Wurman et al. 1996; Wakimoto et al. 2011; Wurman and Gill 2000; Bluestein et al. 2004, 2007b; Wurman and Kosiba 2013). The WEH forms within the tornado core and is likely caused by the centrifuging of hydrometeors and debris (Dowell et al. 2005).

The introduction of polarimetry capabilities has significantly improved our understanding of weather radar

* Current affiliation: GEX Inc., Atkinson, New Hampshire.
+ Current affiliation: Radar Research and Development Division, National Severe Storms Laboratory, Norman, Oklahoma.
# Current affiliation: Department of Geography, Ohio University, Athens, Ohio.

Corresponding author address: Roger M. Wakimoto, Department of Atmospheric and Oceanic Science, University of Colorado, Campus Box 311, Boulder, CO 80309.
E-mail: wakimotoroger@gmail.com

DOI: 10.1175/MWR-D-15-0034.1

scatterers including identifying hydrometeor habits and amounts, distinguishing hail from rain, and discriminating between meteorological and nonmeteorological scatterers (e.g., Vivekanandan et al. 1999; Zrnic and Ryzhkov 1998, 1999). Indeed, Ryzhkov et al. (2005a) presented the first evidence in the refereed literature of a tornadic debris signature (TDS) using a polarimetric radar. They proposed that the TDS is characterized by a strong rotational couplet, a local maximum in radar reflectivity, low differential reflectivity (Z_{DR}), and low cross-correlation coefficient (ρ_{hv}). Tornado debris that is lofted has random orientation, irregular shape, and large size that result in low Z_{DR} and ρ_{hv}. Additional studies suggest that ρ_{hv} provides a better indicator of the presence of tornado debris than Z_{DR} (e.g., Kumjian and Ryzhkov 2008). The latter variable will exhibit a positive bias when rain is present (e.g., Bluestein et al. 2007b) and a negative bias if differential attenuation occurs. There have been several studies that have shown the relationship between TDS identification and tornado detection (e.g., Ryzhkov et al. 2005b; Bluestein et al. 2007b; Kumjian and Ryzhkov 2008; Van Den Broeke et al. 2008; Palmer et al. 2011; Tanamachi et al. 2012; Bodine et al. 2013).

These past studies have provided critical information on the echo structure, velocity fields, and characteristics of the scatterers in and around tornadoes; however, careful analyses of photographs taken at the same time have been relatively rare. Several studies have merged radar reflectivity and Doppler velocity data with tornado photographs in order to elucidate their relationship with the condensation funnel (e.g., Wakimoto and Martner 1992; Wakimoto et al. 2003, 2011, 2012; Dowell et al. 2005; Bluestein et al. 2007a; Rasmussen and Straka 2007; Atkins et al. 2012). To date, however, only the recent study of the Moore tornado (Atkins et al. 2014) has attempted to perform a similar analysis using polarimetric radar data but only in a series of plan plots. Recent numerical simulations have illustrated the complex relationship between the funnel and debris cloud (Lewellen et al. 2008). Debris can affect the wind structure, damage potential, and Doppler radar measurements of the tornado.

On 31 May 2013, a wide and destructive tornado occurred near El Reno, Oklahoma, and resulted in a number of fatalities and injuries. Wurman and Kosiba (2013) and Wurman et al. (2014) have referred to this event as a tornado/multiple vortex mesocyclone. Many of the vortices moved in trochoid-like paths making it challenging at times to differentiate the tornado from suction/subvortices (e.g., Fujita et al. 1976; Fujita 1981; Wurman 2002; Lee and Wurman 2005). Hereafter, these features will be referred to as suction vortices. The El Reno tornado was scanned by the mobile rapid-scanning X-band polarimetric Doppler radar (RaXPol; Pazmany et al. 2013; Snyder and Bluestein 2014; Bluestein et al. 2015) while the evolution of the funnel was captured by a series of photographs and high-definition video. In this paper, radar reflectivity, single-Doppler velocities, Z_{DR}, and ρ_{hv} data are combined with these photographs in order to relate these parameters to the visual characteristics of the tornado. Section 2 presents an overview of the RaXPol radar and photogrammetry techniques used in this study. A brief description of the El Reno tornado and the subsequent ground and aerial damage survey are also discussed. The Twin Lakes, Oklahoma, WSR-88D (KTLX) and RaXPol radar data collected on the tornado are shown in section 3. Section 4 presents the photogrammetric merger of radar data with pictures taken of the El Reno tornado, and section 5 presents an example of low ρ_{hv} ring structures that were observed in several scans recorded by RaXPol. Section 6 discusses the polarimetric detection of pockets of dust/debris that were visually apparent in photographs located in an area south of the funnel. A summary and discussion are presented in section 7.

2. RaXPol, photogrammetry, and overviews of the El Reno tornado and the damage survey

The need for mobile, rapidly scanning radars owing to the evolution of severe storm phenomena has been discussed in the literature (e.g., Bluestein et al. 2001). Accordingly, the Rapid-Scan Doppler on Wheels (RSDOW; Wurman and Randall 2001; Wurman et al. 2014), Mobile Weather Radar 2005 X-band Phased Array (MWR-05XP; Bluestein et al. 2010), Atmospheric Imaging Radar (AIR; Isom et al. 2013), and RaXPol (Pazmany et al. 2013) systems have all been developed and deployed. The RaXPol system is the primary platform used in the present study.

The RaXPol antenna diameter is 2.4 m and transmits at 3.1-cm wavelength. The pedestal rotates the antenna at a maximum rate of $180^\circ s^{-1}$ and the 3 dB (half power) beamwidth is 1°, although the dwell time required to collect samples for moment calculations typically results in an effective beamwidth of ~1.4°. The range resolution during the data collection period was 30 m, oversampled such that the range gates were 15 m. Increasing the number of independent samples needed to calculate the radar parameters while in rapid scan mode is achieved by using the frequency-diversity technique (e.g., Hildebrand and Moore 1990). The interested reader is referred to Pazmany et al. (2013) for additional information on RaXPol.

Photogrammetry has been used to quantitatively analyze pictures of clouds or the condensation funnel

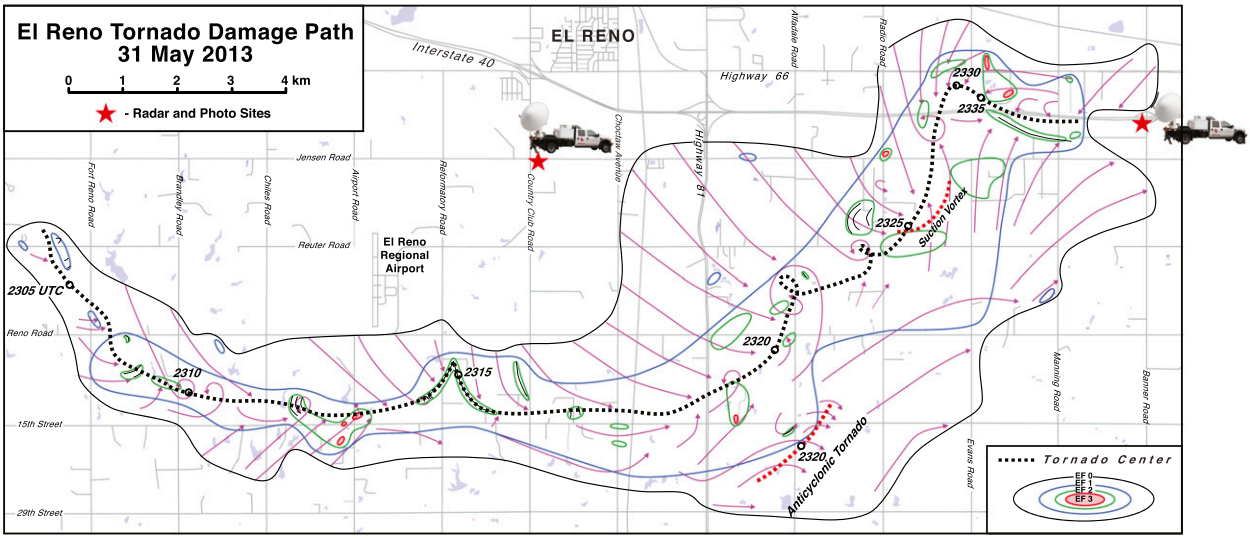

FIG. 1. Damage map of the El Reno, OK, tornado on 31 May 2013. Black, blue, green, and red contours denote the EF-0, -1, -2, and -3 damage intensity isopleths. Black dashed line is the center of the tornado. The two red dashed lines denote the location of an anticyclonic tornado and cyclonic suction vortex. Magenta lines represent the approximate flow as depicted in the damage based on fallen trees, building debris, and streaks in the vegetation based on a detailed aerial survey. Red stars represent two deployment locations of the RaXPol mobile Doppler radar (shown by an icon of the truck). Photographs and videos of the tornado were taken at both sites.

accompanying a tornado (e.g., Malkus 1952; Wakimoto and Martner 1992; Zehnder et al. 2007). The technique requires knowledge of the azimuth angles of targets identifiable on the horizon depicted in a picture and the precise location of the photographer. The effective focal length and the tilt angle of the camera can subsequently be determined using spherical trigonometry. The final step is the creation of an azimuth- and elevation-angle grid that can be superimposed onto the photograph. Comparison of the calculated azimuth-angle grid with the targets visible on the horizon of the picture suggests that errors range between 0.1° and 0.2° (approximately 9–17 m at the distance to the center of the tornado, respectively). An overview of photogrammetry can be found in Abrams (1952) and Holle (1986).

The photographer was located within a few meters of the radar antenna in order to minimize any azimuth-angle errors owing to the photo site and the radar dish being at slightly different locations. It is well known that pictures taken at a wide angle can suffer from distortion at the edges of the image. The two mitigating factors were the high quality of the camera lens that minimizes distortion and limiting the analysis region to, at most, 40% of the total image size centered in the middle of the photograph. The center region of a photograph experiences the least distortion. The radar data were shifted using a time–space conversion before superimposition onto the photograph in order to correct for the motion of tornado in the plane of the photograph. This correction was small since the radar completes 360° in 2 s and a volume contained six elevation angles (0°, 1°, 2°, 3°, 4°, and 5°). The time of the photograph was used as the analysis time.

The approximate collocation of the photographer and radar antenna is important since the azimuth- and elevation-angle grid superimposed onto the photograph will also represent the radar scanning angles. The raw radar reflectivity, Doppler velocities, Z_{DR}, and ρ_{hv} data points at the range to the center of the tornado can be subsequently plotted on the picture. The result is a series of vertical cross sections through the rotational couplet. This technique produces the highest possible resolution since raw rather than interpolated data are used in the analysis.

The synoptic and mesoscale aspects of the storms on 31 May 2013 are detailed in Bluestein et al. (2015). The El Reno storm developed east of the intersection of a dryline with a stationary front (not shown). Extreme potential instability and moderately strong vertical wind shear created a favorable environment for supercell storms and tornadoes. A north-northeast–south-southwest line of intense storms developed at ~2130 UTC (UTC = CDT + 5 h) west and north of the city of El Reno (not shown) in central Oklahoma. The southernmost storm evolved into a supercell and produced a tornado west of the intersection between the Fort Reno and Reuter Roads at ~2303 UTC (Fig. 1). The tornado followed an approximate U-shaped path through primarily rural areas until it dissipated at ~2345 UTC. Ground damage surveys were conducted on 1 and 3 June

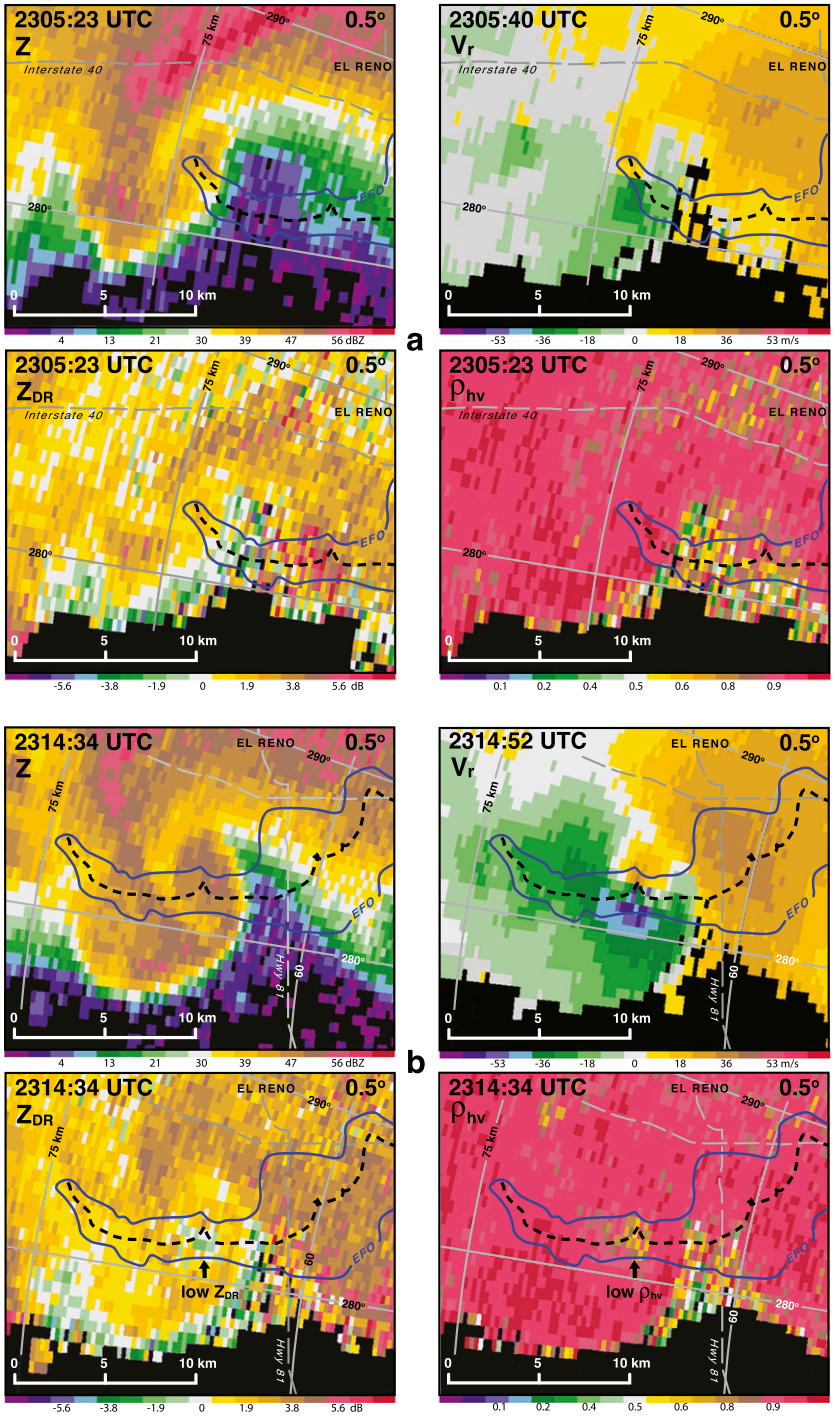

FIG. 2. Low-level scans (0.5°) from the KTLX WSR-88D of reflectivity (Z), Doppler velocities (V_r), differential reflectivity (Z_{DR}), and correlation coefficient (ρ_{hv}) for the (a) 2305, (b) 2314, (c) 2323, and (d) 2332 UTC volume scans. The blue isopleth denotes the EF-0 damage boundary. The black arrow on the Z_{DR} and ρ_{hv} image at 2314:34 UTC denotes areas of low values that suggest lofted debris. The black dashed line denotes the location of the tornado center. The black arrow on the V_r image at 2333:16 UTC denotes the location of an anticyclonic tornado. The dashed gray lines represent major roads. Gray lines represent the range and azimuth angle grid from the KTLX WSR-88D.

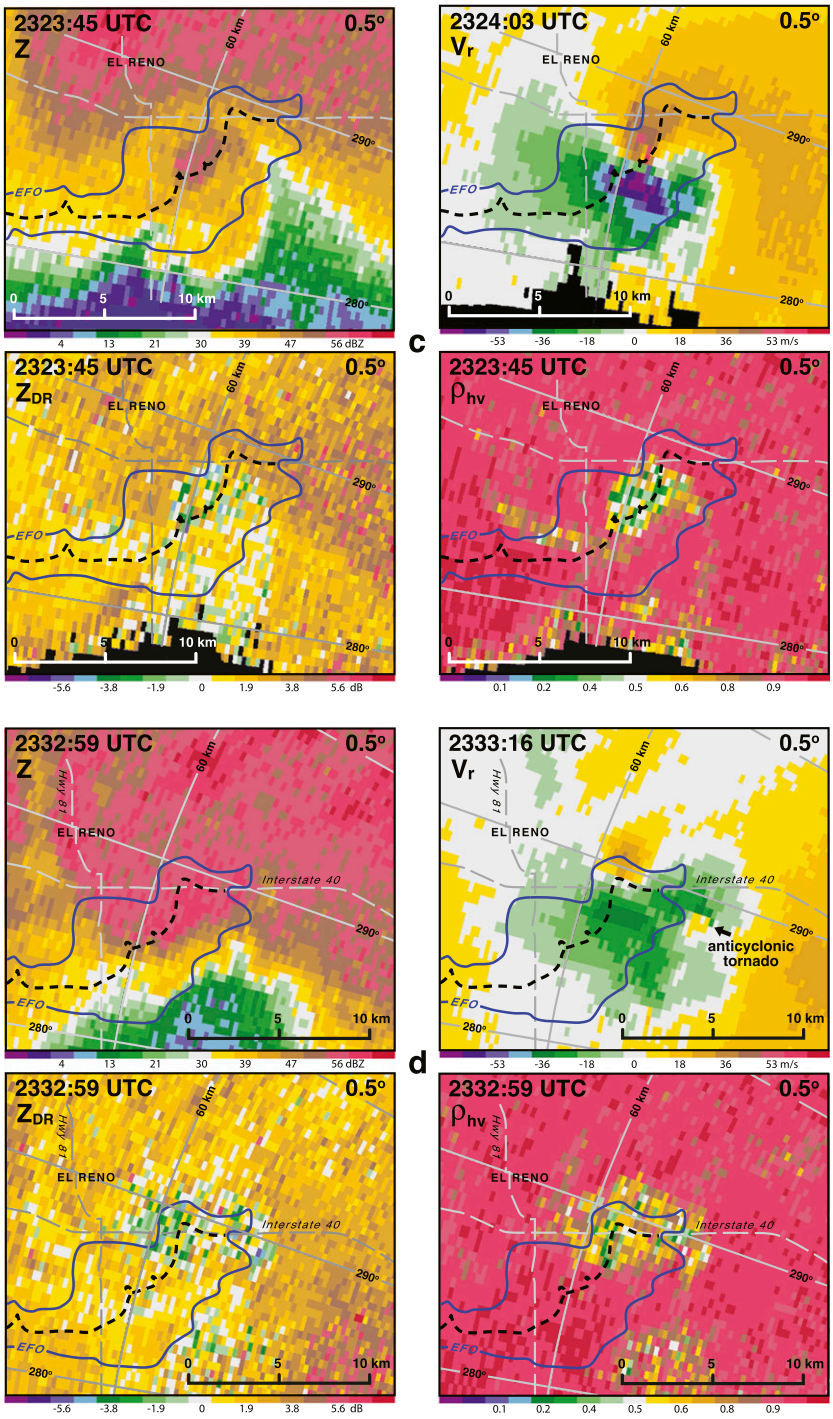

FIG. 2. (*Continued*)

and a comprehensive aerial survey was performed on 4 June. The National Weather Service also provided ground survey estimates of damage in the aftermath of the tornado. The integration of this information led to the map of the El Reno damage path shown in Fig. 1.

Fortunately, the El Reno tornado occurred in a rural area resulting in both fewer structures damaged and people exposed to the strong winds. This is in stark contrast to the Moore tornado that occurred 11 days earlier and damaged more than 4000 structures (e.g., Atkins et al. 2014; Burgess et al. 2014). The absence of

buildings along the tornado's path; however, presented a challenge of accurately estimating the tornado's damage intensity (e.g., Doswell and Burgess 1988; Doswell et al. 2009; Snyder and Bluestein 2014). Aerial and ground surveys confirmed that the structures impacted by the tornadic winds sustained a maximum of EF-3 damage (highlighted by the red shading in Fig. 1) although mobile radar measurements suggested much higher wind speeds located above the surface (Wurman et al. 2014; Snyder and Bluestein 2014; Bluestein et al. 2015). The center of the tornado track was determined by a combination of the aerial survey and the location of the rotational couplet. The overall U-shaped path described earlier is evident in the damage map. The large damage width is also apparent (maximum width ~8 km southeast of El Reno). This large width should not be equated to the tornado's diameter. Some of the damage flow vectors south of the tornado center are suggestive of the rear-flank downdraft (e.g., Lemon and Doswell 1979). Also highlighted on the damage map are the locations of a brief anticyclonic tornado and a cyclonic suction vortex (both indicated by the red dashed line in Fig. 1). Numerous suction vortices were observed in the video recorded by scientific and amateur storm chasers.

The positions of two of the RaXPol deployments are denoted by the red stars on the map. It is the data collected at the eastern site near the off ramp of Interstate 40 and Banner Road that is the focus of the current study. A comprehensive examination of the damage survey conducted in the aftermath of the El Reno tornado combined with mobile rapid scan data from RaXPol and RSDOW will be presented in a companion paper.

3. KTLX and RaXPol radar observations

The relationship between the El Reno damage path and the data recorded by the KTLX radar is shown in Fig. 2. The tornado developed and dissipated at ~75 km and 60 km from the radar, respectively, based on the superposition of the track on top of the images. A weak rotational couplet and a hook echo are apparent early in the tornado's life cycle (Fig. 2a). There is no evidence of a TDS in the Z_{DR} and ρ_{hv} fields owing to the height of the beam above the ground (~1 km) at this distance from the radar. The hook echo is well defined and the rotational couplet has intensified as shown in the 2314 UTC volume scan (Fig. 2b). The first indication of a developing TDS is apparent with low Z_{DR} and ρ_{hv} (black arrows in Fig. 2b) suggesting the presence of lofted debris [also noted by Wurman et al. (2014)].

A large debris signature is evident in the reflectivity scan shown in Fig. 2c with intense echoes centered on the tornado track and a strong velocity couplet. The Z_{DR} and ρ_{hv} signature suggest that the north–south width of the debris field is ~5 km. The radar data depicted in Fig. 2c is close to the times that detailed photogrammetric analyses of the El Reno tornado are performed (section 4). The hook echo is difficult to identify in Fig. 2d when the tornado was crossing Interstate 40. The TDS continues to grow in horizontal dimensions at this time even though the Doppler velocities suggest that the circulation is weakening. This is an example of debris that remains aloft in a strong updraft or is slowly falling to the ground (also referred to as debris fallout) and not necessarily indicative of the tornado's intensity (e.g., Lewellen et al. 2008; Bodine et al. 2013). An anticyclonic rotational couplet associated with a tornado (black arrow in Fig. 2d) is apparent south of Interstate 40 and was discussed by Wurman et al. (2014) and Bluestein et al. (2015).

As previously mentioned, there were two fixed deployment sites of RaXPol during the El Reno tornado as shown in Fig. 1. A series of volume scans were recorded at the eastern site, however, only three of these volumes (2324:45, 2325:00, and 2325:15 UTC) were completed when the radar platform was level. The tornado location at 2325 UTC is labeled along the tornado track in Fig. 1. The tornado was moving northward toward Interstate 40 at this time and was nearing the end of its life cycle. Each volume contained six elevation angle scans (0°, 1°, 2°, 3°, 4°, and 5°). The photogrammetric analysis was restricted to these three times since the merger of radar data with photographs of the tornado requires accurate navigation of both the azimuth and elevation angles. The plan position indicator (PPI) scans at 3° elevation angle for the three times are shown in Fig. 3. The tornado center was located ~5 km from the radar site during this time. The much higher spatial resolution data from RaXPol is apparent when comparing the images in Fig. 3 with Fig. 2c.

A WEH can be clearly identified at 2324:45 UTC (Fig. 3a). Strong rotation is apparent in the Doppler velocity image, but there is also an indication of a smaller TVS embedded within a much larger circulation denoted by the black and white arrows in the figure, respectively. Wurman et al. (2014) noted the same features in their data collected a few minutes earlier. The black arrow in the Z_{DR} image denotes the location of an arc of higher Z_{DR} that is collocated with a region of stronger echoes associated with the hook echo suggesting the presence of hydrometeors (e.g., Palmer et al. 2011).

The TDS is clearly apparent in both the Z_{DR} and ρ_{hv} scans shown in Fig. 3a. The width of the debris field is approximately 2 km based on the ρ_{hv} image. The

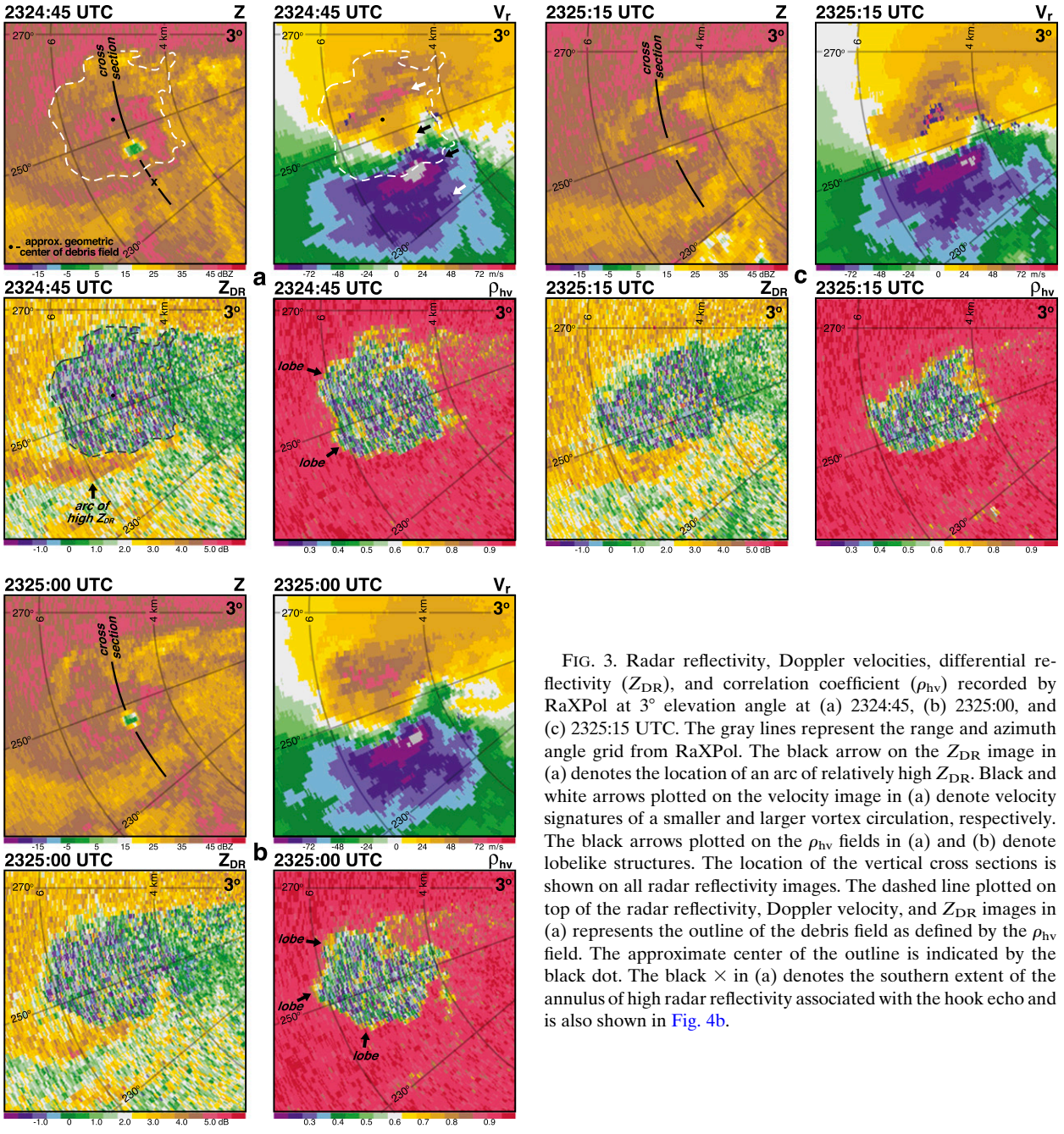

FIG. 3. Radar reflectivity, Doppler velocities, differential reflectivity (Z_{DR}), and correlation coefficient (ρ_{hv}) recorded by RaXPol at 3° elevation angle at (a) 2324:45, (b) 2325:00, and (c) 2325:15 UTC. The gray lines represent the range and azimuth angle grid from RaXPol. The black arrow on the Z_{DR} image in (a) denotes the location of an arc of relatively high Z_{DR}. Black and white arrows plotted on the velocity image in (a) denote velocity signatures of a smaller and larger vortex circulation, respectively. The black arrows plotted on the ρ_{hv} fields in (a) and (b) denote lobelike structures. The location of the vertical cross sections is shown on all radar reflectivity images. The dashed line plotted on top of the radar reflectivity, Doppler velocity, and Z_{DR} images in (a) represents the outline of the debris field as defined by the ρ_{hv} field. The approximate center of the outline is indicated by the black dot. The black × in (a) denotes the southern extent of the annulus of high radar reflectivity associated with the hook echo and is also shown in Fig. 4b.

boundary of the debris field, as defined by the ρ_{hv} field, is outlined by the white dashed line (black dashed line) and is superimposed onto the radar reflectivity and Doppler velocity plots (Z_{DR} plot). The black dot on the image denotes the approximate geometric center of the outlined area. There is a northward displacement of ~1 km between the WEH/center of the rotational couplet and the approximate geometric center of the debris field (black dot). Accordingly, the lofted debris extends into the weak-echo notch of the hook echo. In addition, the northern segment of the outline on the radar reflectivity image is nearly coincident with the southern edge of a strong radar reflectivity gradient. The collocation of the northern extent of the TDS with the radar reflectivity gradient is somewhat surprising and suggests that the debris field might extend farther to the north. One explanation for the collocation of the northern extent of the TDS with the reflectivity gradient is that a combination of heavy rain, hail, and downdrafts has removed the lofted debris in this region. It is also

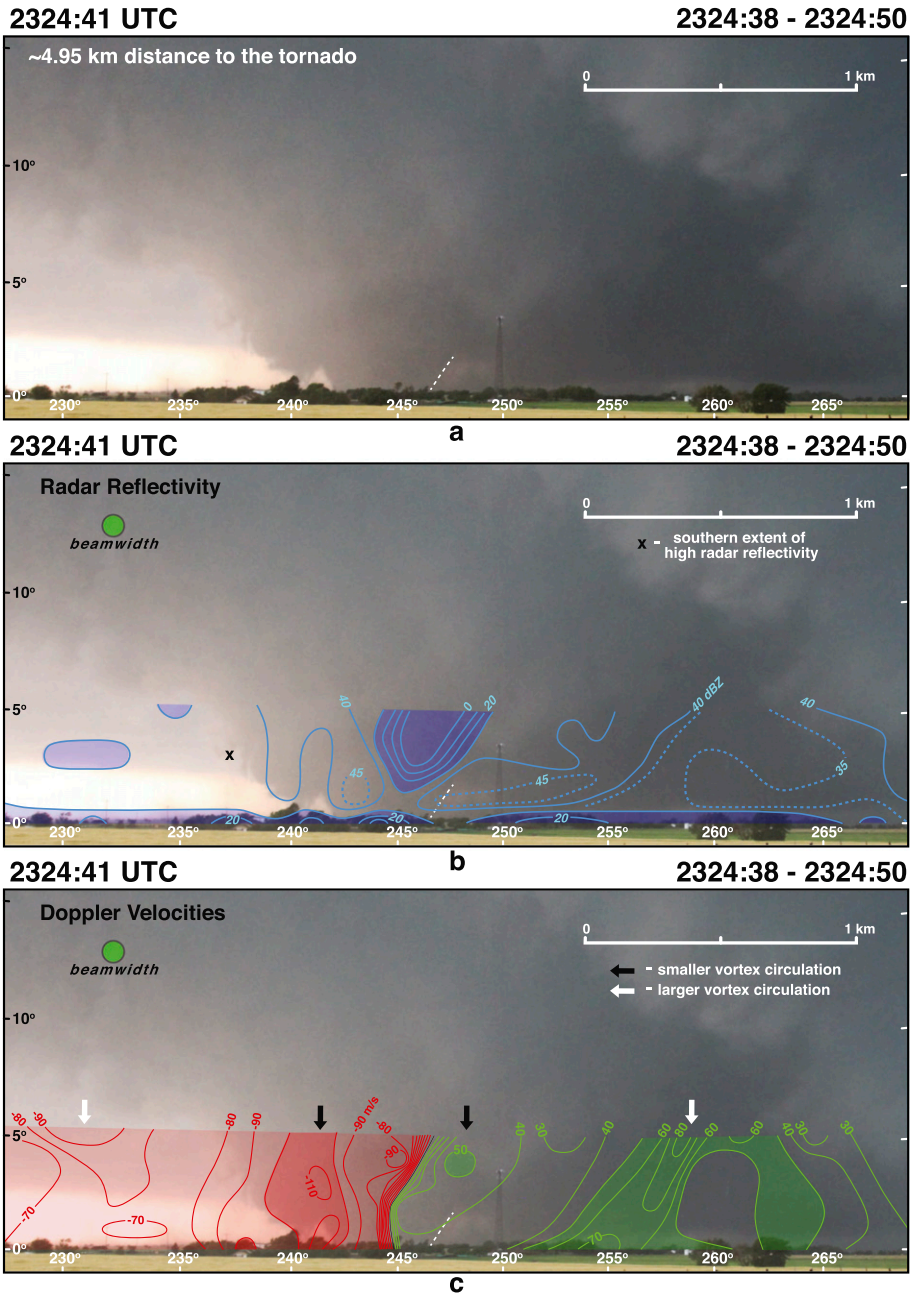

FIG. 4. (a) Wide-angle photograph of the El Reno tornado at 2324:41 UTC. (b) Radar reflectivity (dBZ) from the 2324:38–2324:50 UTC volume scan. Values <30 dBZ are shaded light blue. The 35- and 45-dBZ isopleths have been added as dashed lines in regions characterized by weaker gradients. (c) Ground-relative single-Doppler velocities (m s^{-1}). Red and green lines are isopleths of approaching and receding single-Doppler velocities, respectively. Velocities <-50 and >50 m s^{-1} are shaded light red and green, respectively. Velocities <-100 m s^{-1} are shaded dark red. (d) Cross-correlation coefficient (ρ_{hv}). Values <0.50 are shaded red. (e) Differential reflectivity (Z_{DR}, dB). Red and green lines are isopleths of negative and positive Z_{DR}, respectively. (f) Radar reflectivity and cross-correlation coefficient. The green circle represents the 1° beamwidth of the radar. The scales labeled on the figures are valid at the distance to the center of the tornado. The white dotted line denotes the northern edge of the visible funnel. The black × in (b) denotes the southern extent of the annulus of high radar reflectivity associated with the hook echo and is also shown in Fig. 3a. The black and white arrows in (c) denote velocity signatures of smaller and larger vortex circulations, respectively. The location of the vertical cross section is shown in Fig. 3a.

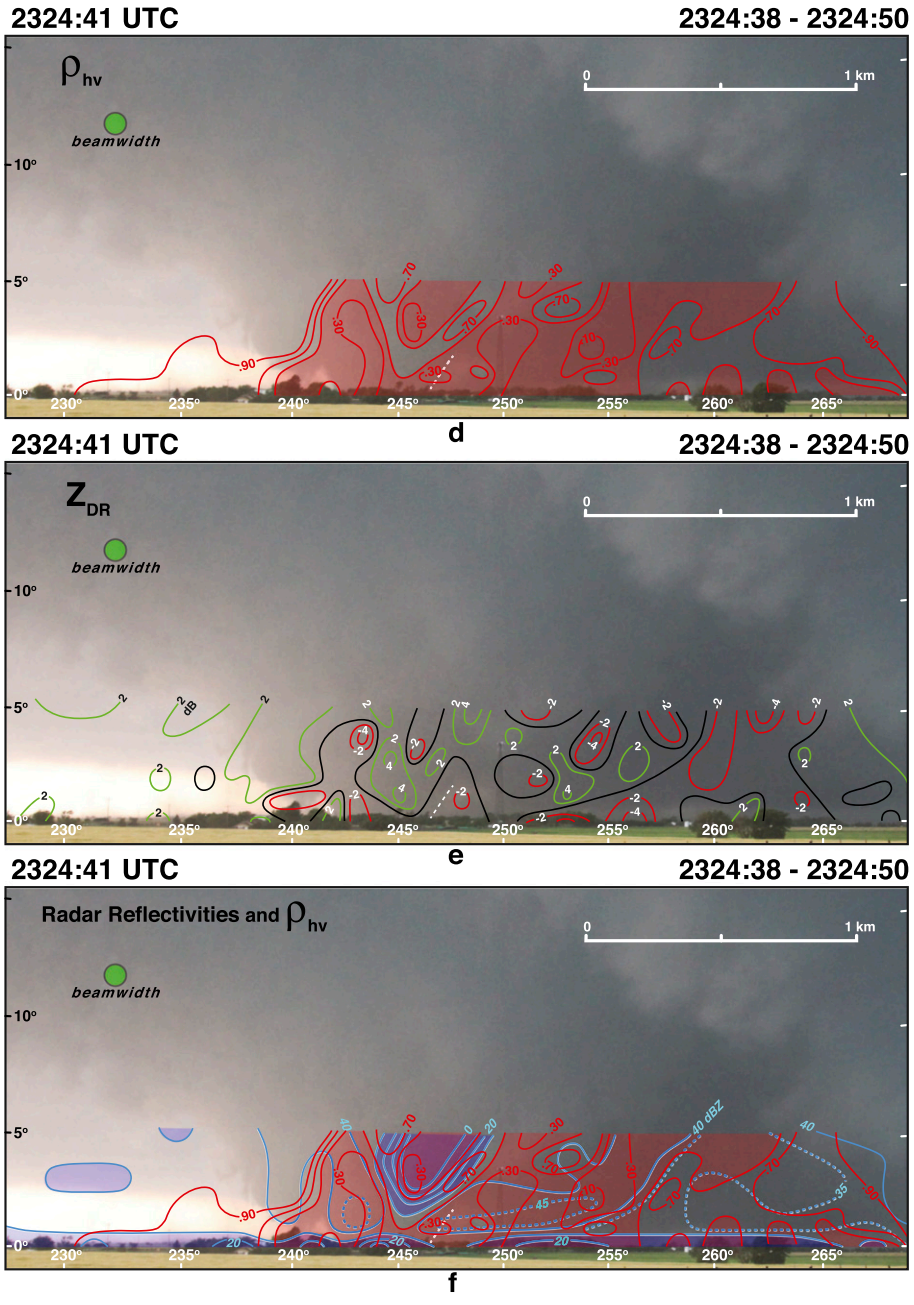

FIG. 4. (*Continued*)

possible that the increase in ρ_{hv} to the north of the TDS is caused by precipitation entrainment associated with the higher echo intensity (e.g., Bodine et al. 2013, 2014). Indeed, although ρ_{hv} will generally decrease in a mixture of debris with hydrometeors (Kumjian and Ryzhkov 2008), an increase in ρ_{hv} can occur if the debris concentration remains the same but the concentration of raindrops increases (Bodine et al. 2013).

The next volume scan at 2325:00 UTC (Fig. 3b) depicts similar kinematic features when compared to the images shown in Fig. 3a. Of particular interest are the lobelike structures that appear in the ρ_{hv} images in Figs. 3a and 3b (highlighted by the black arrows). Lewellen et al. (2008) suggest that a swirling debris flow is highly compressible, which can lead to deviations from symmetry (see their Figs. 1, 3, and 9). It is also possible that these lobelike structures are a result of debris being

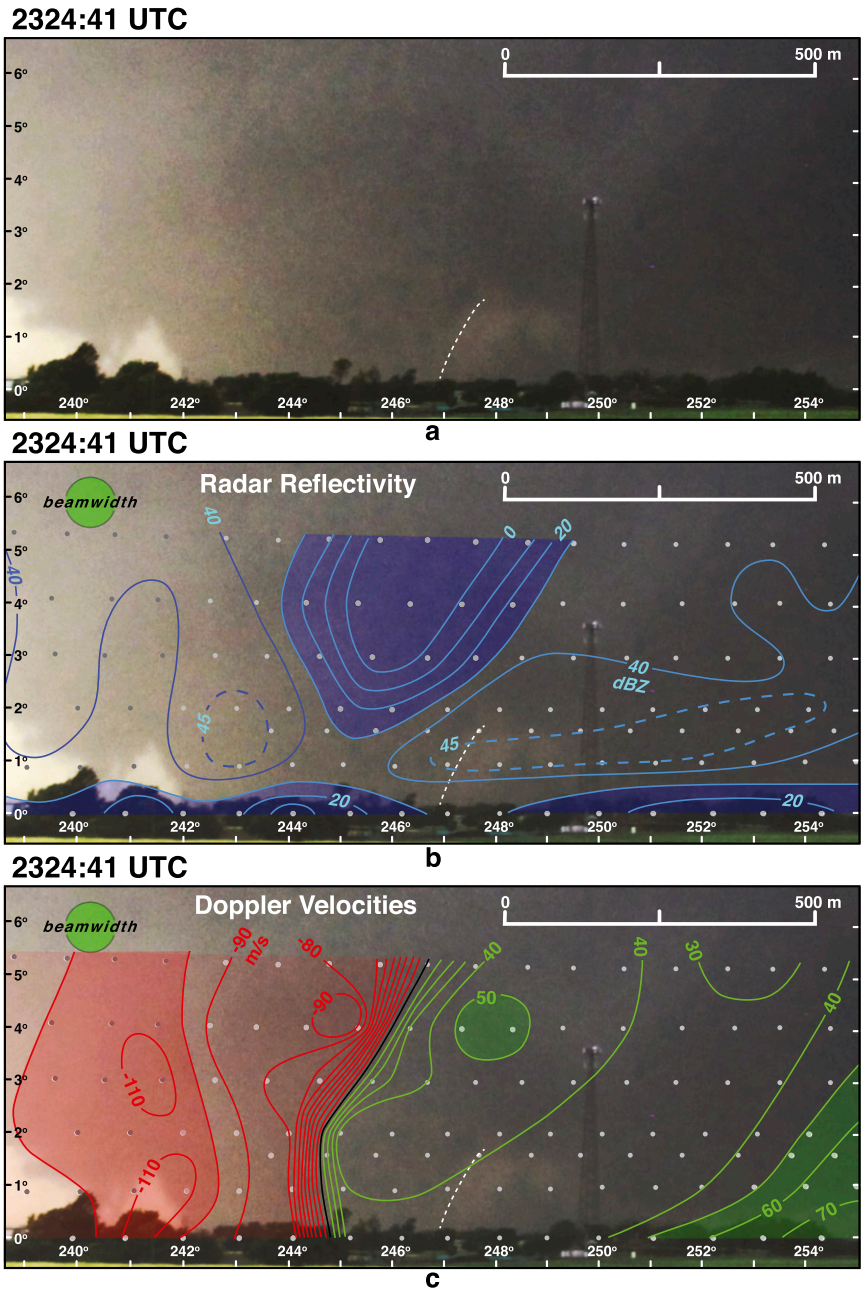

FIG. 5. (a) Enlarged photograph of the El Reno tornado at 2324:41 UTC. (b) Radar reflectivity (dBZ). Values <30 dBZ are shaded light blue. (c) Ground-relative single-Doppler velocities (m s^{-1}). Red and green lines are isopleths of approaching and receding single-Doppler velocities, respectively. Velocities <-50 and >50 m s^{-1} are shaded light red and green, respectively. Velocities <-100 m s^{-1} are shaded dark red. (d) Cross-correlation coefficient (ρ_{hv}). Values <0.50 are shaded red. The 0.20 and 0.40 isopleths have been added (dashed red lines) in areas of weak gradient. (e) Radar reflectivity and cross-correlation coefficient. (f) Radar reflectivity and differential reflectivity (Z_{DR}, dB). Red and green lines are isopleths of negative and positive Z_{DR}, respectively. The green circle represents the 1° beamwidth of the radar. The scales labeled on the figures are valid at the distance to the center of the tornado. The small dots represent the raw data points from RaXPol. The white dotted line denotes the northern edge of the visible funnel. The white dashed line in (e) denotes the location of the horizontal cross section shown in Fig. 7.

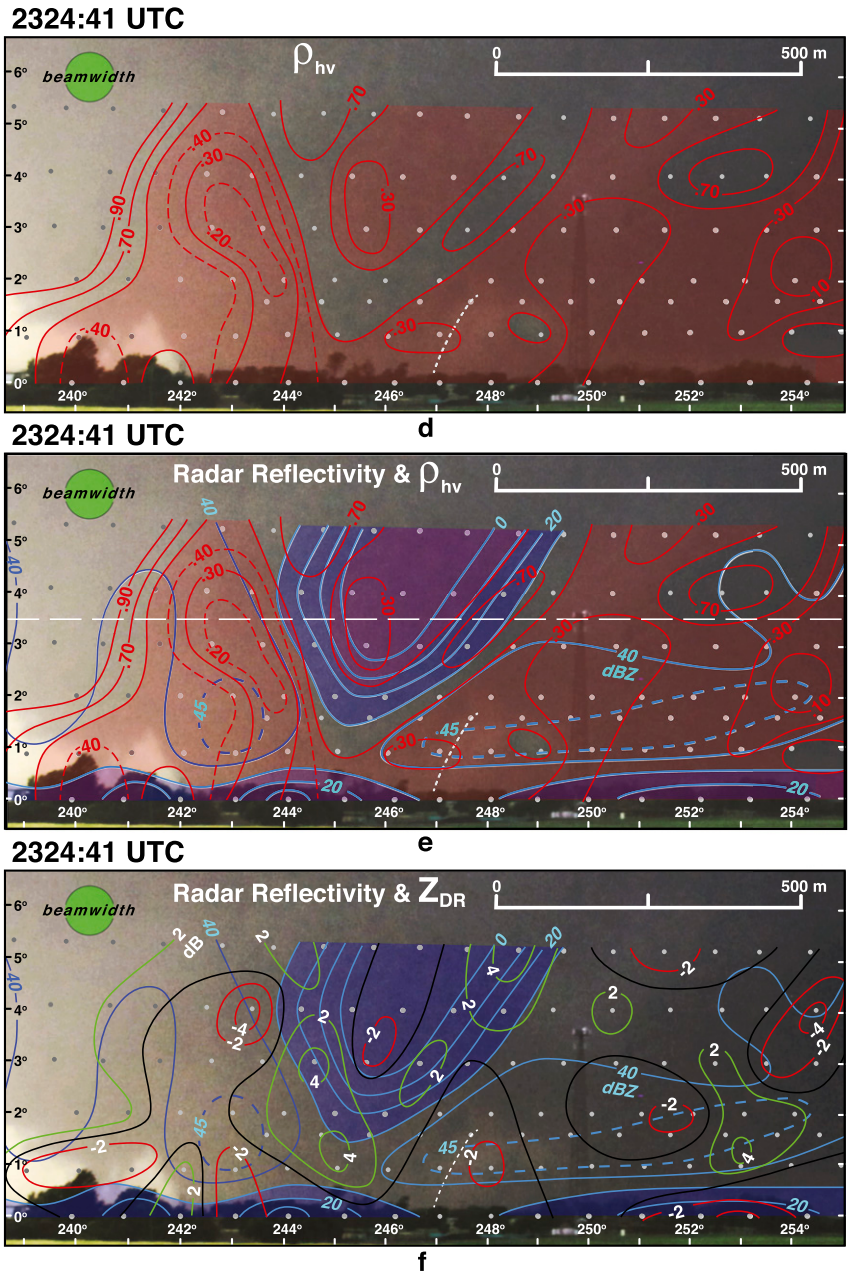

FIG. 5. (*Continued*)

lofted at discreet intervals as the tornado encountered structures built to different construction standards. However, the El Reno tornado was located in an open, rural area at this time suggesting that the latter scenario is less likely. Finally, this pattern could be a result of suction vortices although the lobes are not associated with obvious rotational couplets in the Doppler velocity plots. The images depicted at 2325:15 UTC (Fig. 3c) are different than the earlier volume scans. The WEH is less prominent and the TVS has weakened. The TDS, however, is still prominent in the Z_{DR} and ρ_{hv} scans although the signature is elongated in a west-southwest–east-northeast axis.

4. Vertical cross sections through the tornado

The high spatial and temporal resolution data and polarimetric information afforded by RaXPol provided

an opportunity to document the El Reno tornado's visual structure in relationship to radar reflectivity, Doppler velocity, Z_{DR} and ρ_{hv} fields. The inclusion of vertical profiles of polarimetric data into a photogrammetric analysis has not been previously attempted. The range to the rotational couplet was determined using single-Doppler velocity data from RaXPol. This range, which could vary by a couple of range gates at different elevation angles, was used to construct pseudovertical cross sections through the weak-echo column (WEC)[1] and the rotational couplet using the raw data collected by the radar. These cross sections are along curved surfaces at a constant range as indicated in the radar reflectivity images shown in Fig. 3. The data collected during three consecutive volume scans (2324:38–2324:50, 2324:54–2325:06, and 2325:09–2325:21 UTC) are shown in this section. Partial beam blockage by trees visible in the photographs contributes to the reduced echo intensity at low elevation angles.

a. 2324:38–2324:50 UTC

Two sets of cross sections were created for each of the radar volume scans. One set was a wide-angle view of the entire circulation and lofted debris and a second was an enlarged view of the tornadic circulation. The distance to the center of the tornado was ~4.95 km. The lowered cloud base on the southern part of the storm at ~238° azimuth angle is apparent in Fig. 4a. The southern edge of the funnel was located at 242° (Fig. 5a); however, the northern edge was difficult to discern (denoted by the white dashed line in Figs. 4 and 5). The funnel was ~500 m wide at an elevation angle of 2° (Fig. 5a). The vertical cross section of radar reflectivity superimposed onto the picture of the tornado for the first volume scan is shown in Fig. 4b. Heavy precipitation and lofted debris with radar reflectivities greater than 40 dBZ in this region contributed to the poor visibility (Figs. 4b and 5b). The southern extent of the annulus of high radar reflectivities associated with the hook echo [highlighted by the crisscross ("×") in Fig. 3a] is collocated with the edge of the lowered cloud-base feature in Fig. 4b.

A WEC is apparent (Figs. 4b and 5b) with minimum echo intensity less than 0 dBZ owing to centrifuging of hydrometeors and debris (Dowell et al. 2005). The WEC is qualitatively defined as radar reflectivities less than 40 dBZ and is ~400 m wide at an elevation angle of 5° (blue shading in Fig. 4b). The WEC is not centered in the middle of the funnel at this time and its diameter is less than the width of the funnel, in contrast to the findings shown by Wakimoto et al. (2011) for the LaGrange tornado but consistent with analyses presented by Dowell et al. (2005) and Rasmussen and Straka (2007). The WEC is centered within the velocity couplet where the vorticity is a maximum and the perturbation pressure is a minimum. The displacement of the funnel center from the WEC is likely related to the humidity conditions that may be higher in this northern region. The vertical structure of the WEC is "U shaped" similar to those reported by Wurman and Gill (2000), Dowell et al. (2005), and Wakimoto et al. (2011). The stronger echoes near the surface (~1°) beneath the WEC are the result of lofted debris (Fig. 5b). Dowell et al. (2005) proposed the lofted debris and hydrometeors are centrifuged within a few tens of seconds. This results in a decrease in their number concentration within the tornado core producing the WEC but also an increase in concentration somewhat outside of the core. This model explains the higher radar reflectivities denoted by the 45-dBZ isopleths in regions outside of the WEC especially to the south (Fig. 5b). To the north of the funnel, however, the 45-dBZ isopleth extends from 247° to 254° suggesting that debris is being lofted over greater horizontal distances. However, unlike the region south of the tornado where the region of higher radar reflectivities is nearly collocated with the low values of ρ_{hv}, the area encompassed by the 45-dBZ isopleth north of the tornado is not coincident with a minimum of ρ_{hv}. It is possible that there is a significant amount of hydrometeors mixed in with the debris in this area.

The smaller tornadic vortex embedded within a larger circulation noted in Fig. 3a is apparent in Fig. 4c. The maximum receding velocities associated with the larger circulation at elevation angle 5° are $>80\,m\,s^{-1}$ at 258° azimuth angle and minimum approaching velocities are $<-90\,m\,s^{-1}$ at 231° azimuth angle (shown by the white arrows in the Fig. 4c). The couplet is separated by ~1.9 km resulting in a velocity shear of $\sim 0.09\,s^{-1}$. The black arrows in Fig. 4c (region is enlarged in Fig. 5c) denote the location of the inner couplet associated with the tornado. Minimum and maximum of approaching and receding velocities are <-110 and $>50\,m\,s^{-1}$, respectively. The largest receding and approaching radial velocities associated with the inner circulation are close to the north and south boundaries of the funnel, respectively. The maximum velocity shear in this smaller circulation is $\sim 0.45\,s^{-1}$. Both of the rotational couplets appear to widen with increasing height. The pronounced asymmetry in the circulation is only partially explained by the tornado movement of $\sim 18.6\,m\,s^{-1}$ during this time ($\sim 17\,m\,s^{-1}$ radial component of velocity based on movement of the tornado shown in Fig. 1). It is

[1] Tanamachi et al. (2012) define the weak-echo column as a continuous weak-echo hole in a vertical profile.

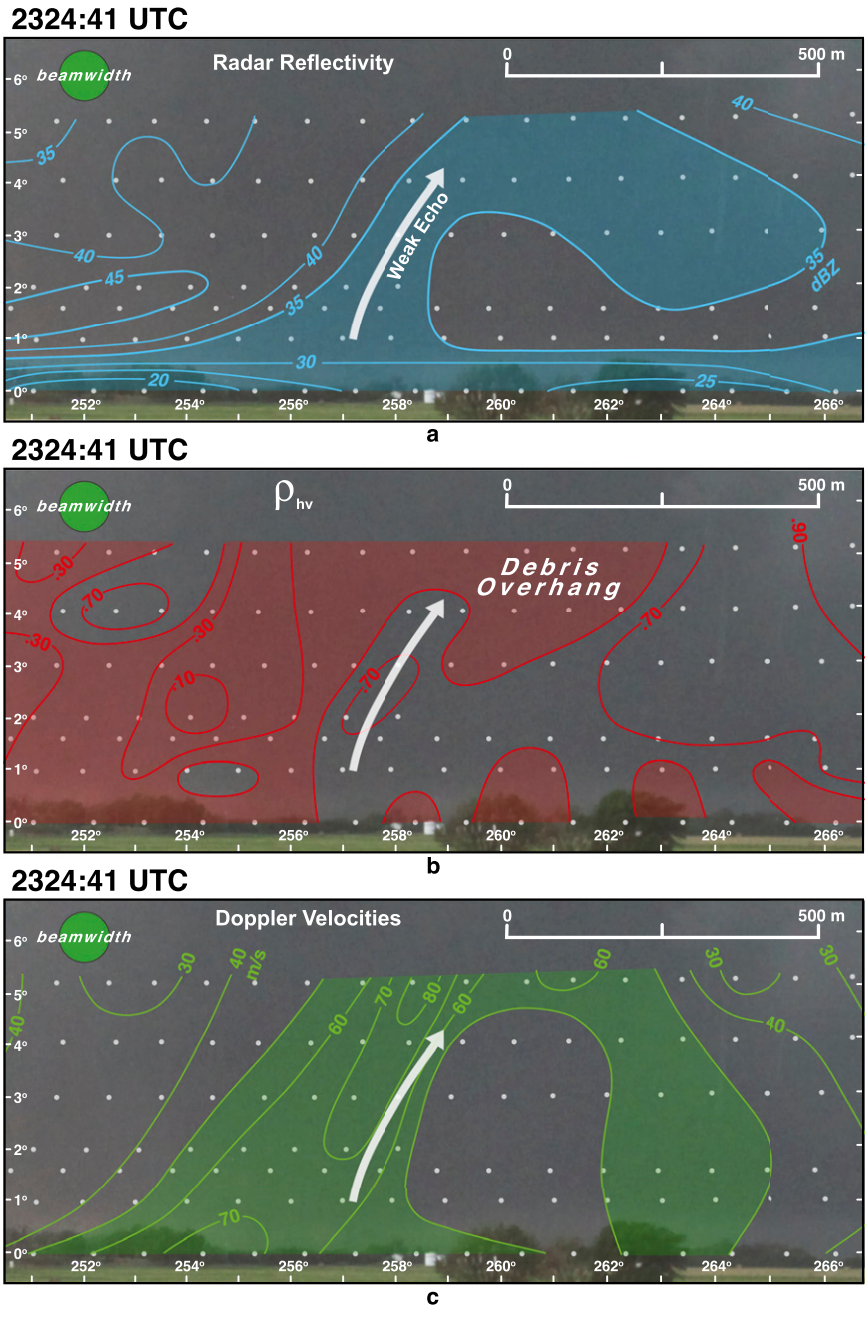

FIG. 6. Enlargement of the debris overhang depicted in Fig. 4. (a) Radar reflectivity (dBZ) with values <35 dBZ shaded blue. (b) Cross-correlation coefficient (ρ_{hv}) with values <0.50 are shaded red. (c) Single-Doppler velocities (m s^{-1}) with values >50 m s^{-1} are shaded light green. White arrow represents the position of the weak-echo trench and "notch" of high ρ_{hv} extending into the debris overhang. The small dots represent the raw data points from RaXPol. The green circle represents the 1° beamwidth of the radar.

possible, however, that the outflow from the rear-flank downdraft is contributing to the asymmetry.

This El Reno storm is an example of the challenge in defining the tornadic circulation. The inner vortex resulted in a damage path that could be tracked over an extended period as shown by the dashed black line in Fig. 1. The larger circulation was associated with wind speeds that meet the criteria for a tornado. Wurman and Kosiba (2013) discussed a similar situation and asked whether this should be classified as a mesocyclone

containing an internal tornado or a tornado with multiple wind speed maxima. The latter may be a more appropriate description in the present case study.

The estimated location of the lofted debris is depicted by the vertical structure of ρ_{hv} (Figs. 4d and 5d; low ρ_{hv} less than 0.50 has been shaded light red). The southern extent of light red shading is located near the edge of the funnel. The debris extends much farther to the north; however, especially aloft (note the shaded area between 257°–262° azimuth and 3°–5° elevation angles) and assumes the shape of a ''debris overhang.'' An enlarged analysis of the overhang is shown in Fig. 6. The overhang is located in a weak echo trench (highlighted by the white arrow in Fig. 6a) and strong receding radial velocities (Fig. 6c). A notch of high ρ_{hv} extends into the overhang (near the tip of the white arrow in Fig. 6b). The overhang, ρ_{hv} notch, echo trench, and strong outbound velocities are consistent with the presence of a nearby updraft. These observations are support the results shown by Bodine et al. (2013). They proposed that centrifuged debris that is small and with low terminal velocity can be recycled and transported vertically by the updraft. The present study suggests that this lofted debris can form an overhang that is detectable in an analysis of the ρ_{hv} fields.

Prominent in the ρ_{hv} field in the vicinity of the funnel is a distinct U-shaped band of higher ρ_{hv} greater than 0.5 (Fig. 5d) positioned along the periphery of the WEC (Figs. 4f and 5d,e). The maximum point value in the band was 0.89. An examination of the vertical cross section of Z_{DR} suggests an approximate U-shaped band of positive values in the same region (Figs. 4e and 5f). The high ρ_{hv} and Z_{DR} suggest the presence of hydrometeors in this U-shaped band and illustrates the complexity of the centrifuging process when hydrometeors and debris are both swirling within a tornadic circulation. Dowell et al. (2005) have examined number concentration of hydrometeors and debris. They show the tendency to produce relatively low concentration inside the vortex core and relatively high number concentration outside the core. The greatest raindrop concentration, however, develops just inside the radius of maximum wind. As the raindrops are lifted, the centrifuging results in the width of the tube of maximum concentration increasing with height. In contrast, centrifuged debris (assumed to be small gravel or small boards) does not reach great heights since they are ejected rather quickly at a height of ~200 m in their simulation (see their Fig. 11). The characteristics of centrifuged debris are also supported by the modeling results presented by Lewellen et al. (2008) for sand particles 0.5 mm in diameter. The simulation by Dowell et al. (2005) suggests that the U-shaped band of relatively high ρ_{hv} located at the periphery of the WEC is the tube of maximum concentration of raindrops.

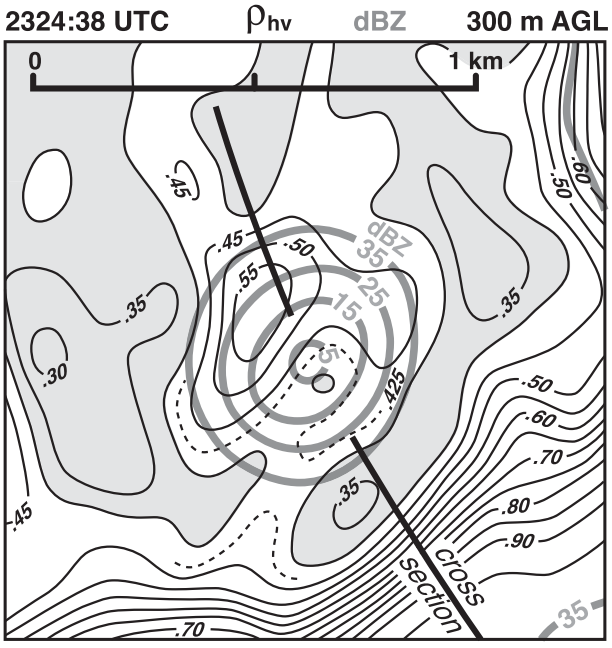

FIG. 7. Plot of radar reflectivity (thick dark gray lines) and ρ_{hv} fields (black lines) centered on the WEH at 300 m AGL at 2324:38 UTC. Values of $\rho_{hv} < 0.40$ are shaded light gray. The 0.425 isopleth (dashed line) is included in a region of weaker gradients. The location of the cross section is shown by the white dashed line in Fig. 5e.

The high spatial resolution of the RaXPol data allows for a finescale examination of the polarimetric characteristics within the WEC. Radar reflectivities within the WEC are less than 0 dBZ, the minimum in ρ_{hv} is less than 0.30 (the lowest raw data point was 0.12), and Z_{DR} was slightly negative. This combination of variables suggests that the WEC is composed of a low concentration of very small, randomly oriented debris particles and an absence (or low concentration) of hydrometeors. Lewellen et al. (2008) note that the central core is sporadically populated by sand even in the presence of strong centrifuging.

The horizontal structure of ρ_{hv} through the WEH at 300 m is presented in Fig. 7. The RaXPol data were interpolated onto a 30-m horizontal grid using a two-pass Barnes's scheme (Koch et al. 1983). The filter was chosen based on the data resolution, δ (30 m). The smoothing parameter κ was 0.006 km^2 [$\kappa = (1.33\delta)^2$]. A ρ_{hv} minimum is evident in the interpolated data near the minimum radar reflectivities. Higher values of ρ_{hv} nearly encircle the minimum followed by an extensive area of low ρ_{hv} at larger radial distances from the WEH.

Similar structures using polarimetric observations have been reported previously in the literature. Kumjian and Ryzhkov (2008) presented a schematic model that

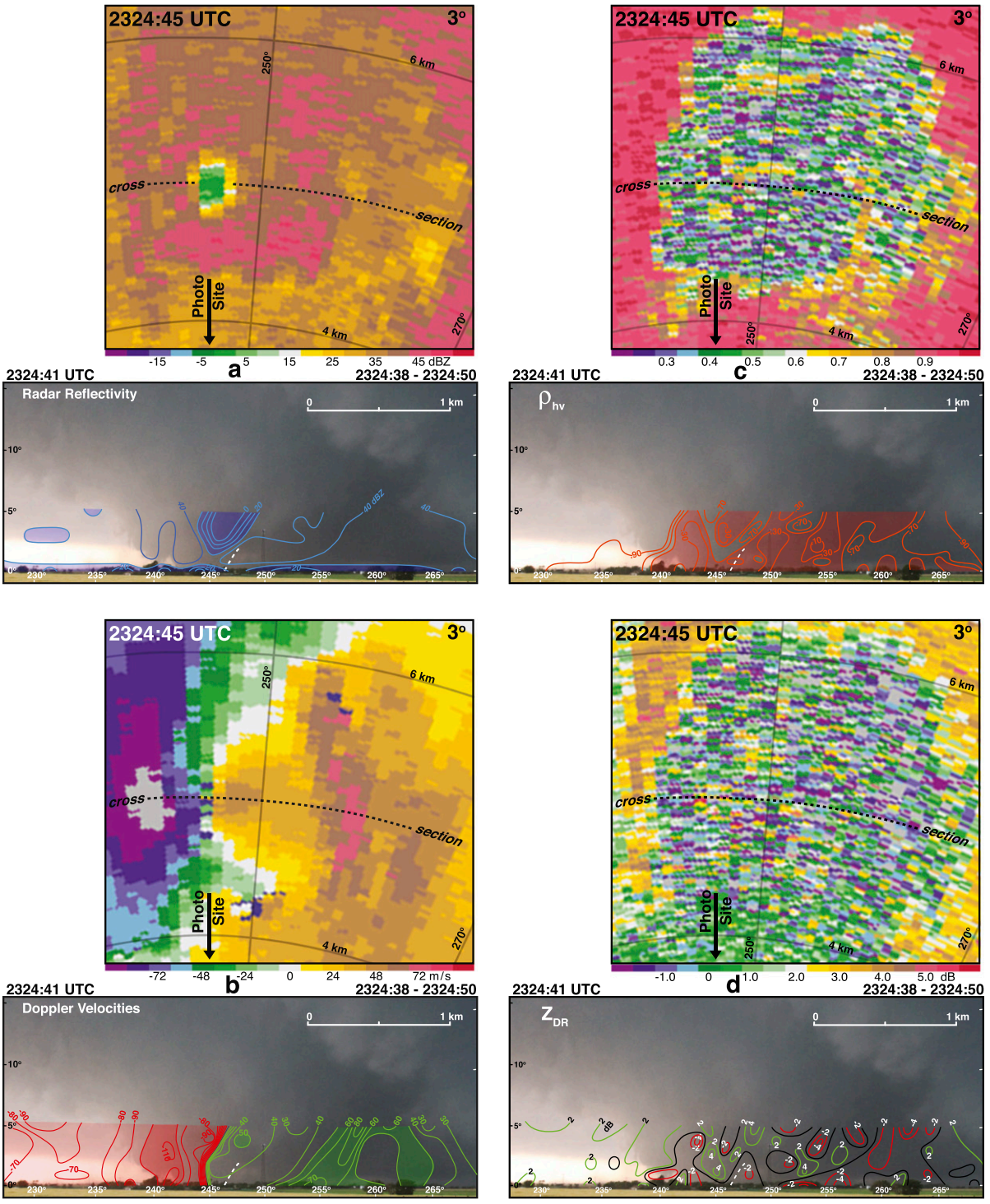

FIG. 8. Photogrammetric cross sections and plan position indicator (PPI) scans at an elevation angle of 3° for the 2324:38–2324:50 UTC volume scan. (a) Radar reflectivity, (b) Doppler velocities, (c) cross-correlation coefficient (ρ_{hv}), and (d) differential reflectivity (Z_{DR}). Radar reflectivity <30 dBZ is shaded light blue. Red and green lines are isopleths of approaching and receding single-Doppler velocities, respectively. Velocities <-50 and >50 m s^{-1} are shaded light red and green, respectively. Velocities <-100 m s^{-1} are shaded dark red. Cross-correlation coefficient less that 0.50 is shaded red. Length scale on the photogrammetric analyses is valid at the distance to the center of the tornado and matches the length scale for the PPI scan. The white dotted line denotes the northern edge of the visible funnel. The location of the photogrammetric cross section is shown by the dashed line on the PPI scans. The gray lines on the RaXpol scans represent the range and azimuth-angle grid.

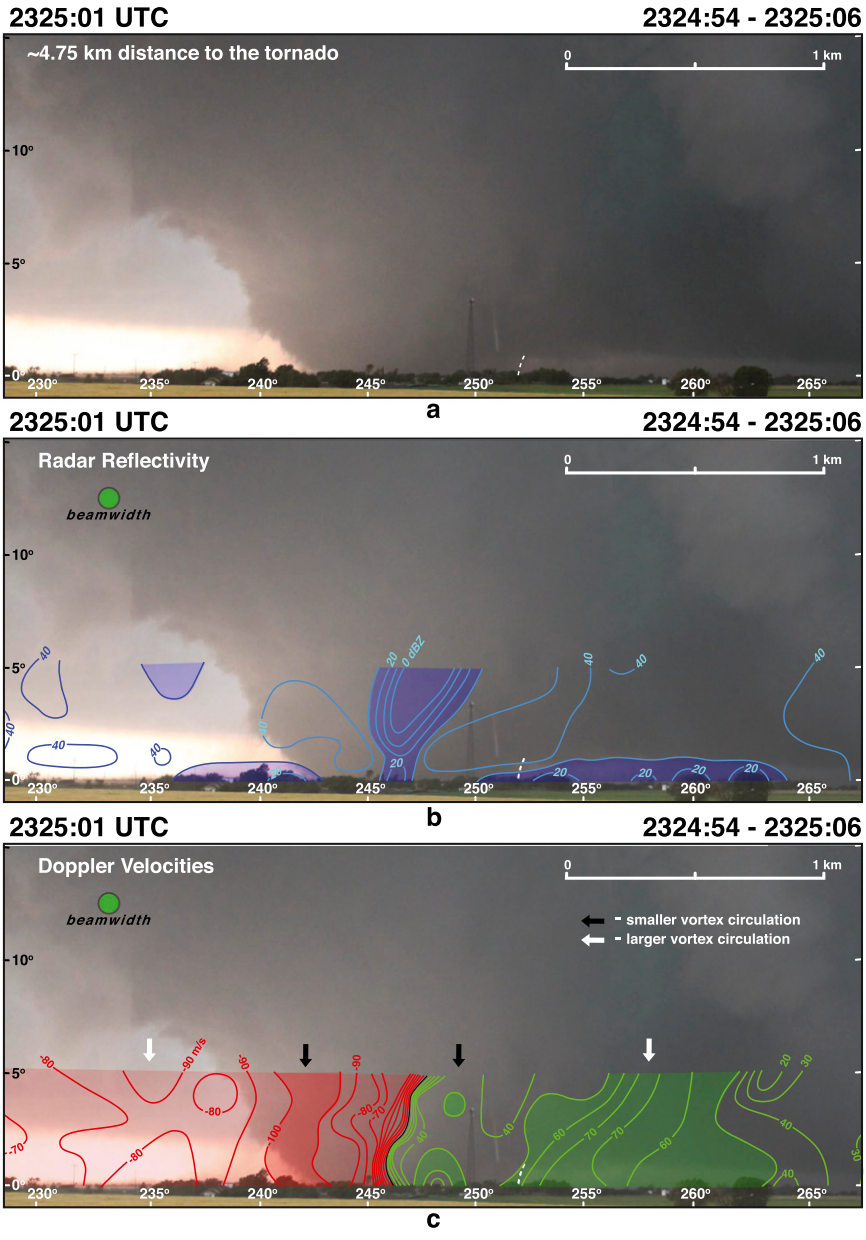

FIG. 9. (a) Wide-angle photograph of the El Reno tornado at 2325:01 UTC. (b) Radar reflectivity (dBZ) from the 2324:54–2325:06 UTC volume scan. Values <30 dBZ are shaded light blue. (c) Ground-relative single-Doppler velocities (m s^{-1}). Red and green lines are isopleths of approaching and receding single-Doppler velocities, respectively. Velocities <-50 and >50 m s^{-1} are shaded light red and green, respectively. Velocities <-100 m s^{-1} are shaded dark red. (d) Cross-correlation coefficient (ρ_{hv}). Values <0.50 are shaded red. (e) Differential reflectivity (Z_{DR}, dB). Red and green lines are isopleths of negative and positive Z_{DR}, respectively. (f) Radar reflectivity and cross-correlation coefficient. The green circle represents the 1° beamwidth of the radar. The scales labeled on the figures are valid at the distance to the center of the tornado. The white dotted line denotes the northern edge of the visible funnel. Black and white arrows in (c) denote velocity signatures of a smaller and larger vortex circulation, respectively. The location of the vertical cross section is shown in Fig. 3b.

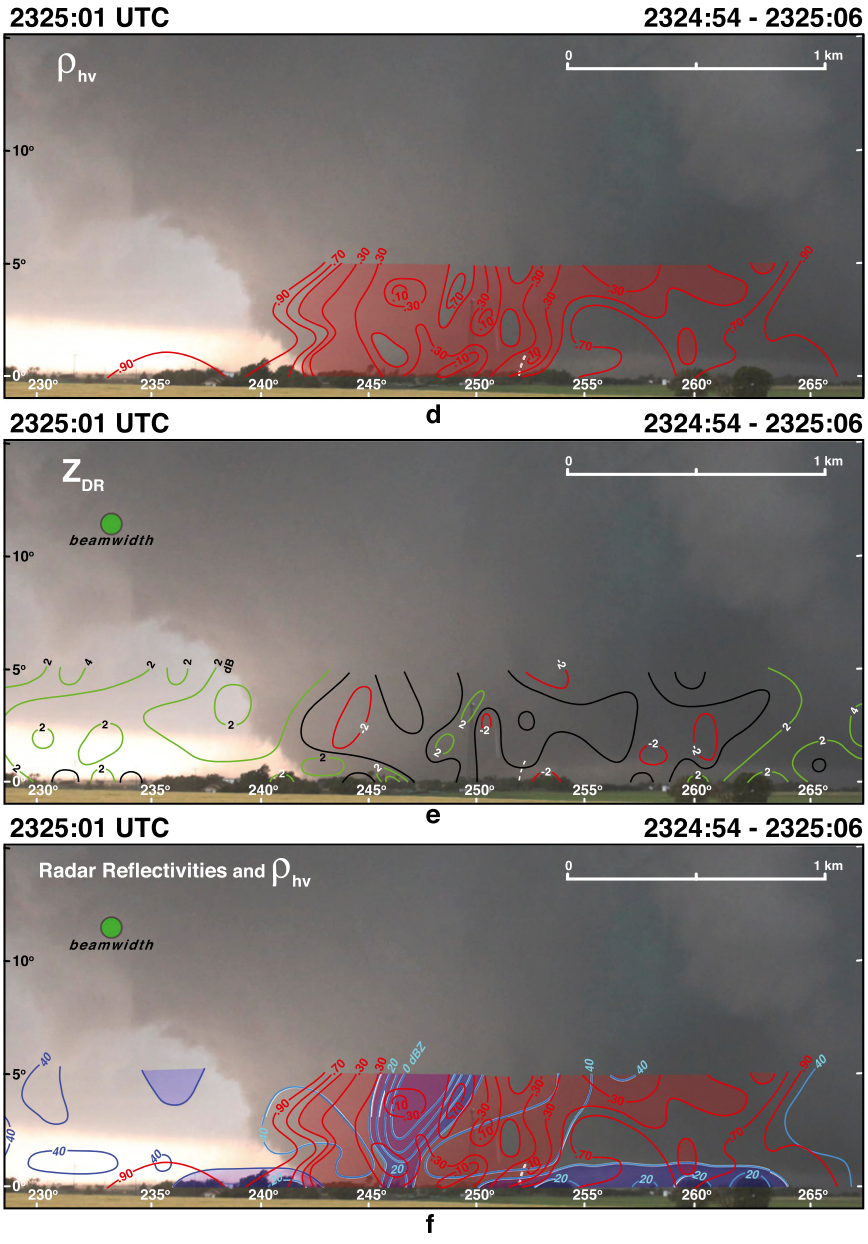

FIG. 9. (*Continued*)

showed rings of enhanced Z_{DR} and reduced ρ_{hv} in a weak-echo region but confined to the main rotating updraft, not the tornado. In addition, the rings in their studies were located near and above the freezing level. Tanamachi et al. (2012) also examined Z_{DR} and ρ_{hv} rings within a tornadic supercell but with insufficient resolution to determine the polarimetric characteristics within and surrounding the WEH. Bodine et al. (2014) created a set of schematics for a polarimetric TDS for several levels (see their Fig. 12). Near the surface (110 m), a maximum of radar reflectivity from debris scatterers is centered on a broad minimum of ρ_{hv}. A ρ_{hv} maximum is within the WEH at higher levels (720 m). The polarimetric data apparent at the 1° and 2° elevation angles shown in Fig. 5 approximately agree with the model presented by Bodine et al. (2014); however, a ρ_{hv} minimum within the WEH at higher levels has not been previously documented in the literature.

The RaXPol PPI scans at an elevation angle of 3° were magnified and rotated to closely match the viewing angle of the photographer in order to further elucidate the relationship between the vertical and horizontal

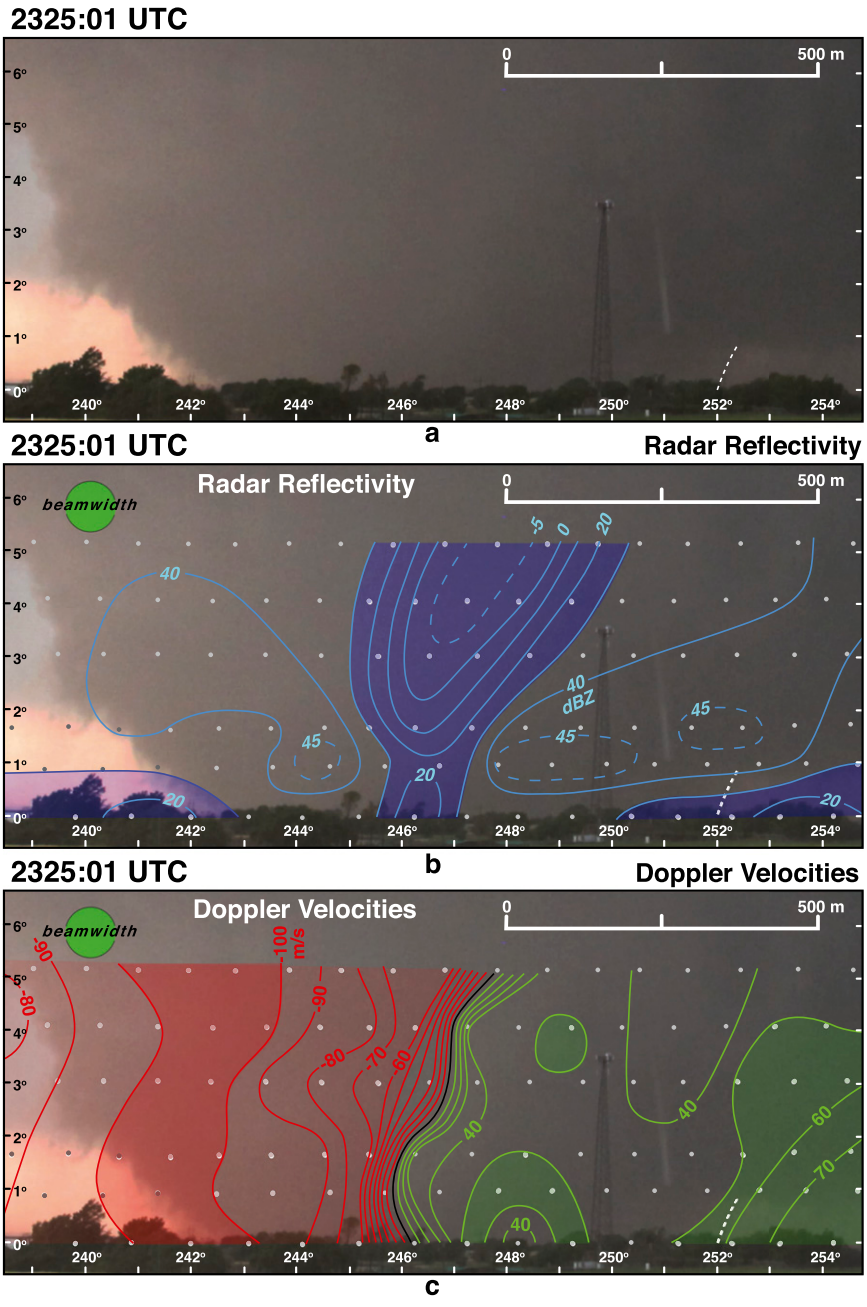

FIG. 10. (a) Enlarged photograph of the El Reno tornado at 2325:01 UTC. (b) Radar reflectivity (dBZ). Values <30 dBZ are shaded light blue. (c) Ground-relative single-Doppler velocities (m s^{-1}). Red and green lines are isopleths of approaching and receding single-Doppler velocities, respectively. Velocities <-50 and >50 m s^{-1} are shaded light red and green, respectively. Velocities <-100 m s^{-1} are shaded dark red. (d) Cross-correlation coefficient (ρ_{hv}). Values <0.50 are shaded red. (e) Radar reflectivity and ρ_{hv}. (f) Radar reflectivity and differential reflectivity (Z_{DR}, dB). Red and green lines are isopleths of negative and positive Z_{DR}, respectively. The green circle represents the 1° beamwidth of the radar. The scales labeled on the figures are valid at the distance to the center of the tornado. The white dotted line denotes the northern edge of the visible funnel. The white arrows in (d) denote two areas near the WEC where ρ_{hv} is >0.50. The small dots represent the raw data points from RaXPol.

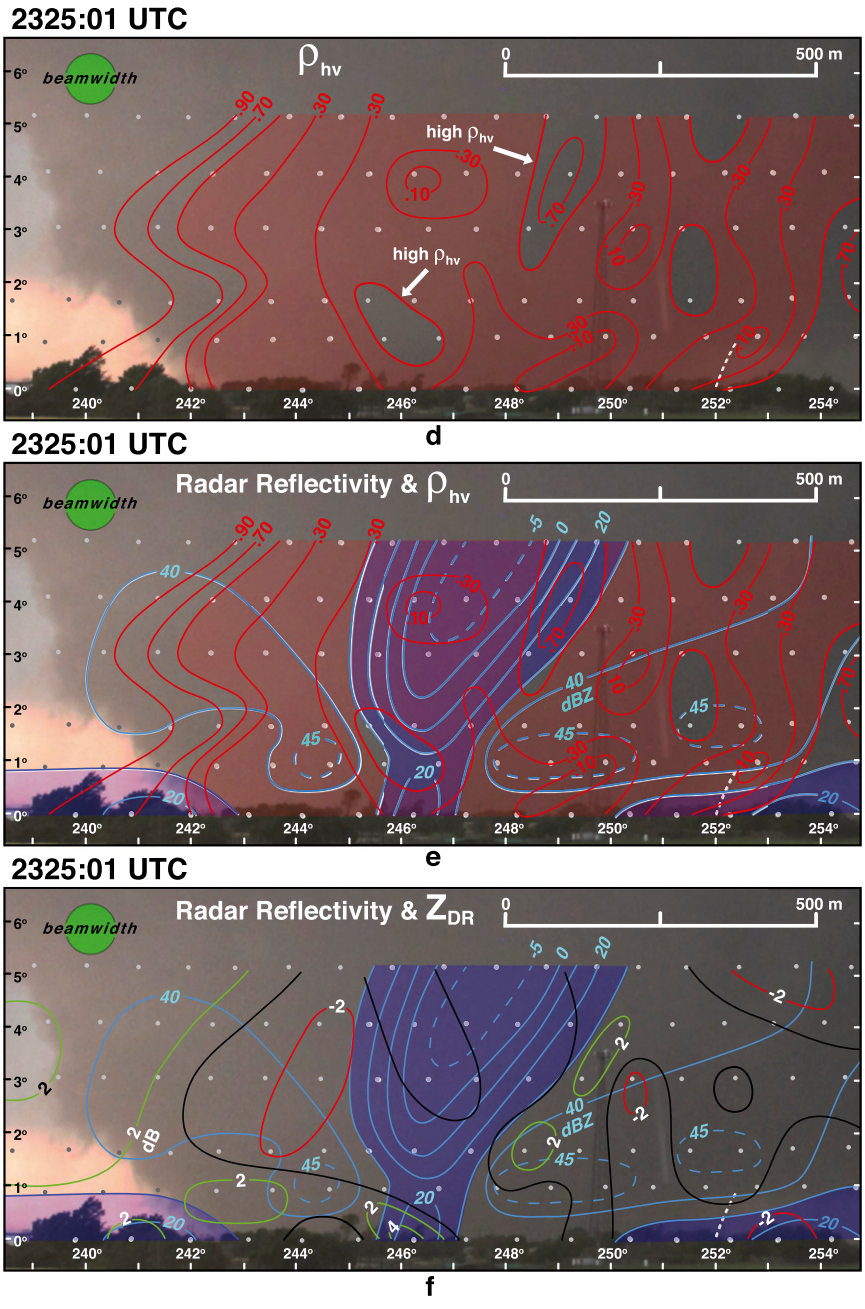

FIG. 10. (*Continued*)

structure of radar reflectivities, Doppler velocities, ρ_{hv}, and Z_{DR} with the tornado. The photogrammetric analyses presented in Figs. 4b–e were reduced in size so the length scale shown on these plots matched those presented in the radar scans to facilitate direct comparisons. The rotation of the radar scans closely aligns the azimuth angles with the photogrammetric cross sections in Fig. 8. The tube of high reflectivity in the PPI scan surrounding the tornado is illustrated in Fig. 8a. The horizontal and vertical structure of the debris field as defined by the ρ_{hv} and Z_{DR} analyses (Figs. 8c,d) and its relationship to the hook echo (Fig. 8a) is apparent in the figure. The impressive expanse of the debris field, especially to the north and west (Fig. 8c) when compared with the positions of the WEH (Fig. 8a), weak echo notch, and intense rotational couplet (Fig. 8b) is also evident. The debris overhang (Fig. 8c) is located north of the hook echo (Fig. 8a) and within a broad region of

intense, receding Doppler velocities associated with the larger circulation (Fig. 8b).

b. 2324:54–2325:06 and 2325:09–2325:21 UTC

The funnel width has increased dramatically by the next analysis time (2324:54–2325:06 UTC) and is ~800 m in diameter (Figs. 9a and 10a). The WEC is still clearly defined and centrifuging of debris and hydrometeors has resulted in minimum reflectivities below −5 dBZ (Figs. 9b and 10b). The WEC is now approximately centered within the funnel in contrast to the earlier time. Stronger echoes (>45 dBZ) form an annulus around the WEC between 1° and 2° (Fig. 10b). The rotational velocities have weakened during this volume scan for both the larger and smaller circulations (Fig. 9c denoted by the white and black arrows, respectively, and Fig. 10c). The TDS is still apparent in the fields of ρ_{hv} and Z_{DR} (Figs. 9d and 9e, respectively). The debris overhang remains a prominent feature from 254° to 262° (Fig. 9d) and is located within the weak echo trench (Figs. 9b,f), consistent with the previous volume scan.

The major change in the analyses of the polarimetric fields is the absence of the U-shaped band of relative high ρ_{hv}. Instead, two regions with values greater than 0.50 are apparent centered at ~246° and 249° that are located at the periphery of the weak-echo column (white arrows in Fig. 10d). These areas are located near regions of positive Z_{DR} (Fig. 10f). These observations highlight the rapidly evolving nature of the hydrometeor and debris field within the El Reno tornado and suggest that the band can be a transient feature without a continued influx of hydrometeors as proposed by Dowell et al. (2005). Low ρ_{hv} and Z_{DR} (Figs. 10e and 10f) are still apparent within the WEC consistent with the previous analysis time.

There is a pronounced weakening of velocity gradients within the tornado during the next volume scan (2325:09–2325:21 UTC; Fig. 11c) even though the magnitudes of the velocities are still strong. Striking when comparing the plot shown in Fig. 4c with Fig. 11c is the dramatic change from asymmetric to axisymmetric flow. The maximum outbound wind speed is 80 m s^{-1} and the maximum inbound wind speed is 110 m s^{-1} (Fig. 11c). As previously noted, the motion of the tornado was ~17 m s^{-1} toward the radar during the data collection period. The rapid evolution in the kinematic structure of the tangential flow in ~30 s highlights the importance of rapid updates provided by mobile radar platforms. The weaker velocity gradients lead to a reduction in the centrifuging effect and a less-pronounced WEC (Fig. 11b). The overall TDS pattern is similar to earlier analysis times, including the presence of the debris overhang (not shown).

5. Observations of ringlike structures

There were a few scan times when rings of low ρ_{hv} were observed in the RaXPol data. An example is shown in Fig. 12. The data shown in this figure were collected when RaXPol was positioned near the intersections of Country Club and Jensen Road (Fig. 1). The track of the El Reno tornado was largely over a rural area, however, there were a few structures that were impacted by the high winds. The center of the tornadic circulation (Fig. 12c) was positioned near a damaged house rated EF-3 (the red shaded area located east of the 2312:55 UTC time stamp in Fig. 12a). The small area of high radar reflectivities (~48 dBZ), indicated by the black arrow in Fig. 12b, is likely the result of the lofted debris from this damaged structure. Indeed, a weak-echo hole was collocated with the center of the rotational couplet during the earlier volume scan at 1° elevation angle at 2315:44 UTC when the tornado was located west of the house (not shown). The gray circle superimposed on the scans of ρ_{hv}, radar reflectivity, and Doppler velocities (Fig. 12d) denote the position of a ringlike region of relatively low cross-correlation coefficient. The blue dashed line encompasses a region of relatively high radar reflectivity (Fig. 12b) and is transposed onto the ρ_{hv} image (Fig. 12d). The area enclosed in the latter image is dominated by high ρ_{hv} and relatively high Z_{DR} (not shown). Accordingly, it is possible that the ringlike structure of low ρ_{hv} could be partially attributable to an increased concentration of hydrometeors (approximately enclosed by the dashed line) inside the ring that has resulted in larger ρ_{hv} even if the debris concentration remains relatively constant (Bodine et al. 2013). It is also possible that the low ρ_{hv} ring represents a trajectory of debris being shed from the northeastern side of the tornado. Additional studies are needed to understand the mechanisms that produce ringlike structures in ρ_{hv}.

6. Dust/debris patterns at the periphery of the tornado

It is common to identify isolated pockets of lofted dust/debris near the funnel in photographs owing to the strong, swirling winds associated with the tornado or wind gusts associated with the rear-flank downdraft. In the present case, high-resolution video and still images of the El Reno tornado revealed organized patterns of lofted dust/debris located south of the funnel. An example of dust/debris pockets is highlighted by the black arrows superimposed onto the image at 2324:41 UTC (Fig. 13a). Note that one of these clusters is located at 232° and is positioned ~750 m to the south of the funnel. A vertical cross section of data collected by

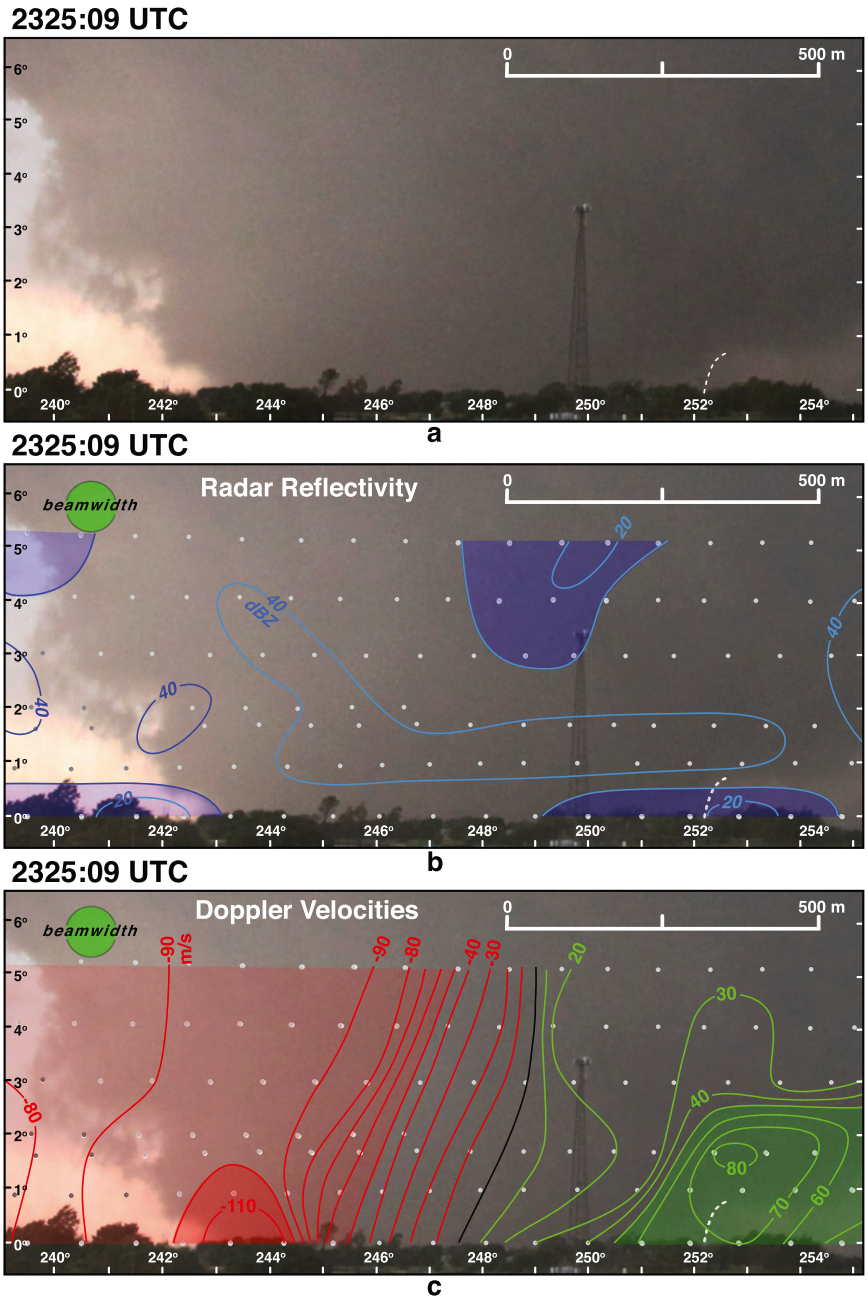

FIG. 11. (a) Enlarged photograph of the El Reno tornado at 2325:09 UTC. (b) Radar reflectivity (dBZ). Values <30 dBZ are shaded light blue. (c) Ground-relative single-Doppler velocities (m s^{-1}). Red and green lines are isopleths of approaching and receding single-Doppler velocities, respectively. Velocities <-50 and >50 m s^{-1} are shaded light red and green, respectively. Velocities <-100 m s^{-1} are shaded dark red. The green circle represents the 1° beamwidth of the radar. The scales labeled on the figures are valid at the distance to the center of the tornado. The white dotted line denotes the northern edge of the visible funnel. The small dots represent the raw data points from RaXPol.

RaXPol at the range of the tornado illustrates that the Doppler velocities and the radar reflectivities were generally between 70–80 m s^{-1} and 30–40 dBZ, respectively, near these clusters (Fig. 13b). The low radar reflectivities near the surface (shaded blue) were caused by partial beam blockage. The prominent features in Fig. 13c are two troughs of ρ_{hv} (black dotted lines) that approximately overlap with the dust/debris clusters. The

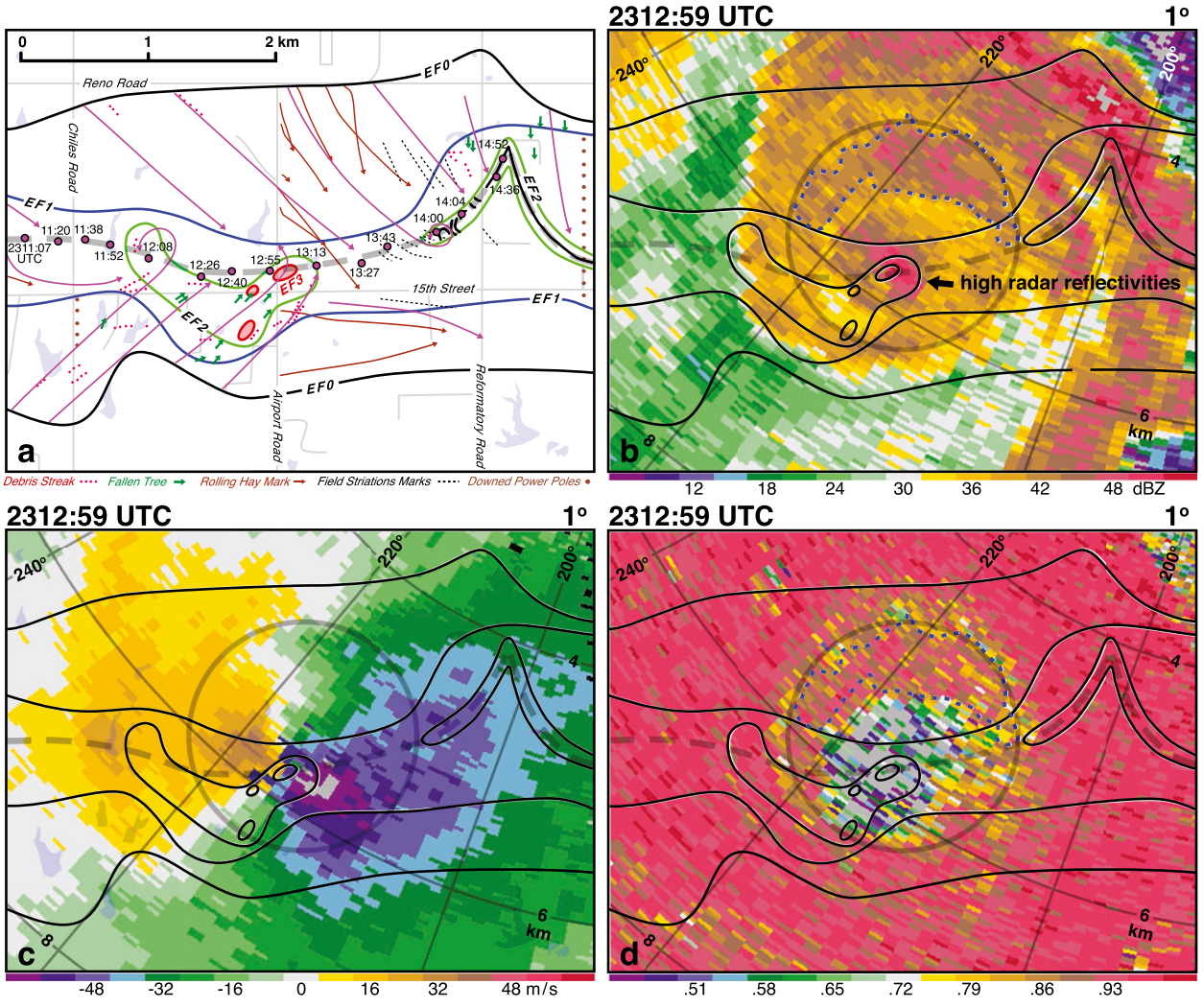

FIG. 12. (a) An enlargement of the El Reno damage map. The EF isopleths are drawn. The circles represent the location of the center of the rotational couplet at the indicated times (in minutes and seconds). Dashed gray line denotes the center of the tornado track. Magenta lines represent the approximate direction of the flow based on debris streaks, fallen trees, rolling bales of hay, and striations marks in the fields. A legend for the markings is provided at the bottom of the figure. (b) Radar reflectivity scan at 1° from RaXPol at 2312:59 UTC. (c) Doppler velocity scan at 1° from RaXPol at 2312:59 UTC. (d) Cross-correlation coefficient scan at 1° from RaXPol at 2312:59 UTC. Black arrow in (b) denotes a region of enhanced radar reflectivity. Gray circle in (b),(c), and (d) denotes the location of a ringlike feature characterized by relatively low ρ_{hv}. The center of the tornado track and the EF isopleths are superimposed onto the radar images in (b),(c), and (d). The gray lines in (b),(c) and (d) represent the range and azimuth-angle grid from RaXPol.

general range of ρ_{hv} in these regions is 0.80–0.95, which is not as low as those associated with the El Reno TDS. It is interesting to note that the region near the surface between the two clusters is associated with weaker Doppler velocities $> -70\,\mathrm{m\,s^{-1}}$ (black arrow in Fig. 13b) as might be expected. While the ρ_{hv} fields show promise in highlighting regions characterized by small dust/debris clusters, there is no apparent signature in Z_{DR} analysis presented in Fig. 13d. This supports past studies that have highlighted the importance of ρ_{hv} when delineating lofted debris.

An enlargement of the RaXPol PPI scan at 2324:40 UTC south of the tornado at 1° elevation angle is presented in Fig. 14. The color scale in Fig. 14a was adjusted to emphasize ρ_{hv} in the range depicted in the photogrammetric analysis (Fig. 13c). Indeed, this change to the color plot shows several areas suspected of being debris clusters that were not evident in the radar scan presented in Fig. 3a. The region of relatively low ρ_{hv} denoted by the middle arrow (Fig. 14a) is the dust/debris area that appears between 234° and 236° in the vertical cross section (Fig. 13c). It is more difficult to detect the trough in ρ_{hv} that is located between 231° and 232° in Fig. 14a since ρ_{hv} is higher and the gradients are weaker (Fig. 13c). Moreover, the 1° scan is above the region of

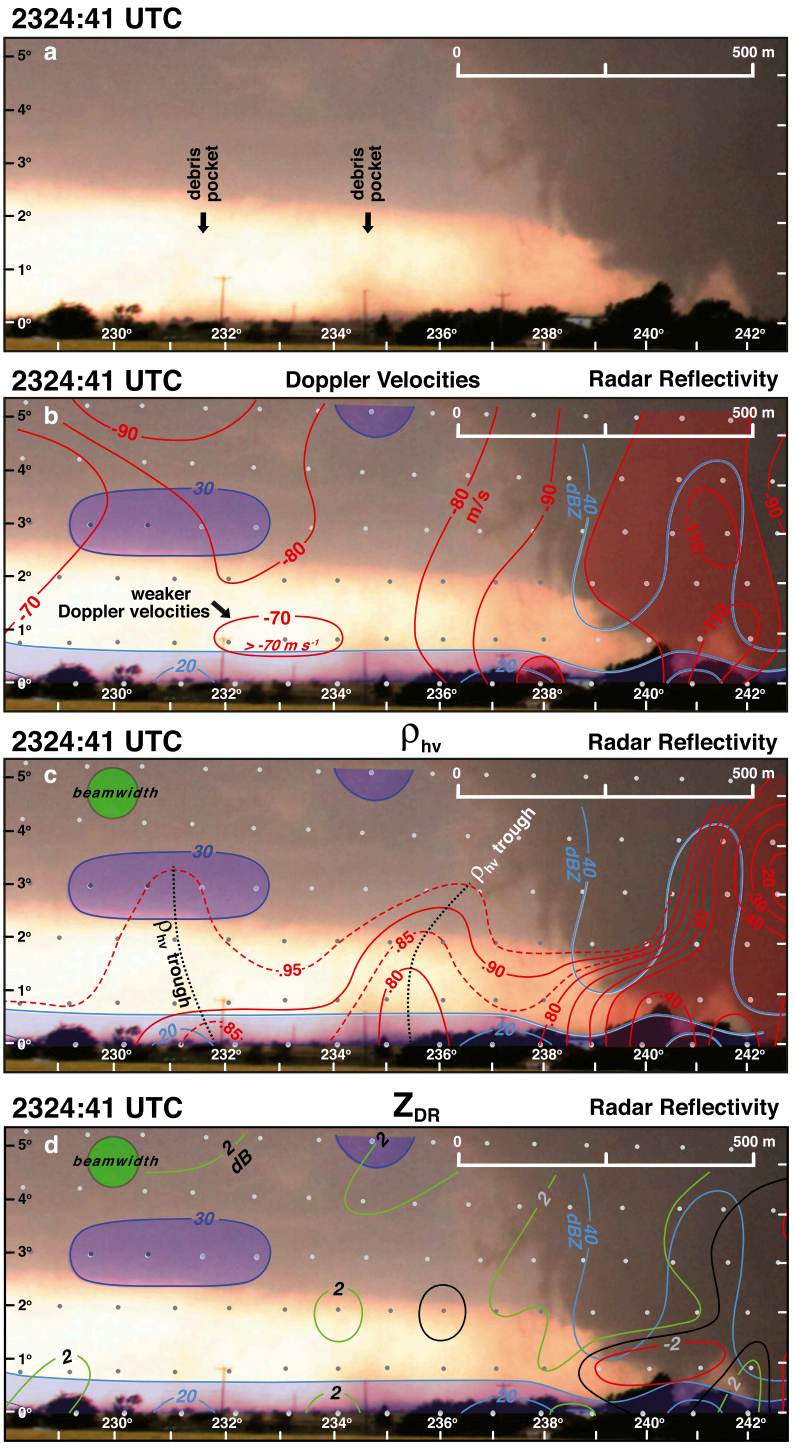

FIG. 13. (a) Photograph of the region south of the El Reno tornado at 2324:41 UTC. (b) Radar reflectivity (dBZ) and single-Doppler velocities ($m\,s^{-1}$). (c) Radar reflectivity (dBZ) and cross-correlation coefficient (ρ_{hv}). (d) Radar reflectivity (dBZ) and differential reflectivity (Z_{DR}, dB). Radar reflectivity <30 dBZ are shaded light blue. Red lines in (b) are isopleths of approaching Doppler velocity with values $<-100\,m\,s^{-1}$ are shaded red. The black dotted lines in (c) denote two troughs in ρ_{hv}. Cross-correlation coefficient in (c) <0.50 are shaded red. The 0.85 and 0.95 isopleths of ρ_{hv} in (c) have been added (dashed red lines) in regions of weaker gradients. The green circle represents the 1° beamwidth of the radar. The scales labeled in the figures are valid at the distance to the center of the tornado. The small dots represent the raw data points from RaXPol.

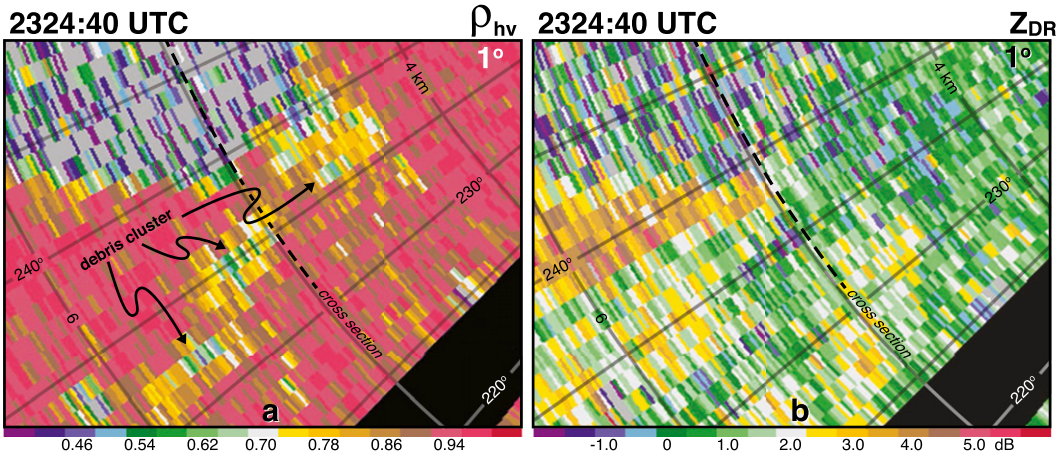

FIG. 14. PPI scan of (a) cross-correlation coefficient (ρ_{hv}), and (b) differential reflectivity (Z_{DR}) recorded by RaXPol at 1° elevation angle at 2324:40 UTC. The arrows in (a) indicate relative low ρ_{hv} that suggest the presence of "debris clusters." The location of the photogrammetric cross section is shown by the dashed line. The gray lines represent the range and azimuth-angle grid from RaXPol.

minimum ρ_{hv}. There does not appear to be an obvious signature in the Z_{DR} scan that would suggest the presence of clusters of dust/debris (Fig. 14b).

7. Summary and discussion

A detailed analysis of the radar data collected by RaXPol combined with cloud photography was performed on the El Reno tornado on 31 May 2013. The relationship between the hook echo, weak-echo hole (WEH), weak-echo column (WEC), and rotational couplet with the visual characteristics of the tornado were shown. For the first time, this study also incorporated cross-correlation coefficient (ρ_{hv}) and differential reflectivity (Z_{DR}) data. The El Reno tornado was accompanied by a large tornadic debris signature (TDS) with a diameter ~2 km wide during the analysis time. The geometric center of the TDS was not collocated with the WEH and center of the rotational couplet. Instead, the TDS was displaced ~1 km to the north and within the weak-echo notch of the hook echo, most likely because the centrifuged debris was small, had low terminal fall velocity and was recycled within the updraft. Vertical cross sections revealed the large region of lofted debris within and surrounding the tornado. Highlighted in the analysis was an area of debris located well above the surface that was referred to as a "debris overhang." The overhang was located in a weak-echo trench where a suspected updraft could suspend small debris particles associated with low terminal velocities. Also apparent was a notch of relatively high ρ_{hv} that help delineate the position of the updraft. A U-shaped band of high ρ_{hv} and Z_{DR} was resolved within the tornadic circulation during the first volume scan. The band was located at the periphery of the WEC. It is hypothesized that the band formed as a result of an increased concentration of hydrometeors (and some debris) encircling the WEC. This feature was transient since only two segments of the U-shaped band were resolved in the subsequent volume scan. This type of evolution is possible without a continued influx of hydrometeors.

The high-resolution data collected by the mobile radar resulted in a detailed examination of the polarimetric characteristics of the scatterers within the WEC. The radar reflectivities, ρ_{hv}, and Z_{DR} were <0 dBZ, <0.50, and <0 dB, respectively, within the WEC. This suggests that the WEC was composed of a low concentration of very small, randomly oriented, debris particles and a general absence of hydrometeors even in the presence of strong centrifuging effects. Isolated pockets of lofted dust/debris south of the tornado were identified in both high-definition video and photographs. These pockets were detectable as troughs in the ρ_{hv} analysis. These debris clusters could also be identified in the low-level PPI scans.

A summary of the debris and hydrometeor pattern for the El Reno tornado at 2324:41 UTC is illustrated in a schematic model (Fig. 15). The hook echo, WEH, and WEC and their relationship with the tornado are depicted in both the three-dimensional and vertical cross section. The yellow circles represent hydrometeors that encircle the WEC. Debris particles within and surrounding the tornado are shown including the northward displacement of the lofted debris into the weak-echo notch of the hook echo. The updraft results in a debris overhang of relatively small debris particles in the schematic. The updraft was inferred based on the debris overhang, weak-echo trench, and ρ_{hv} notch, and

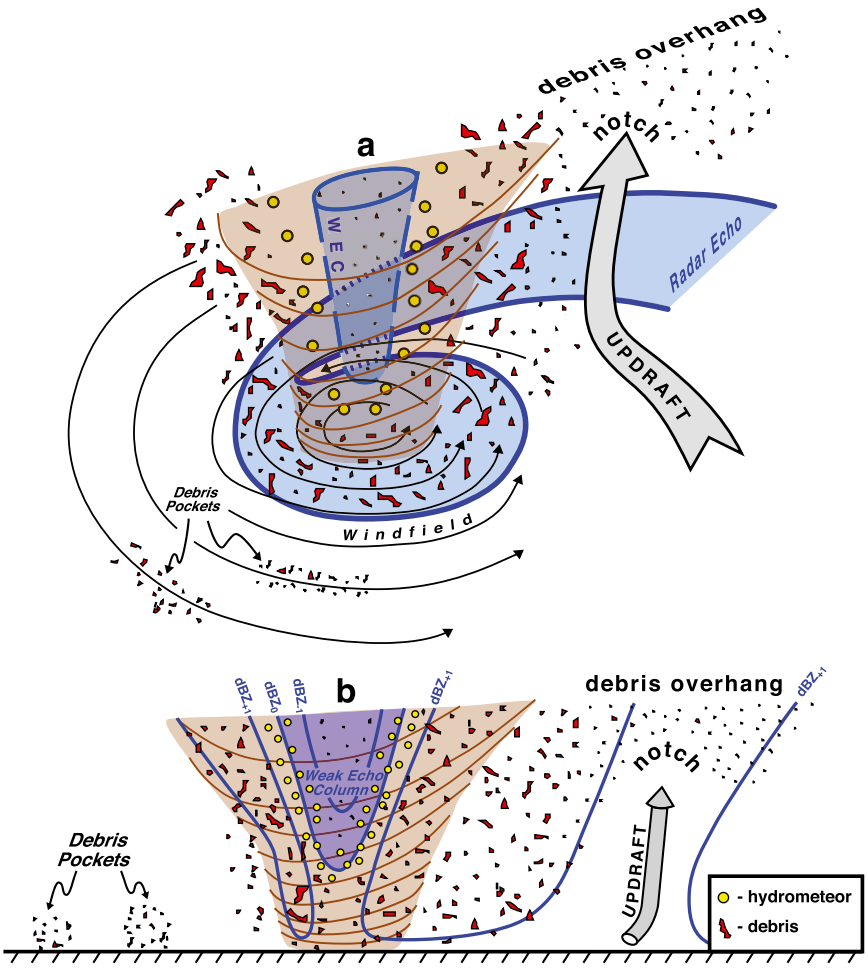

FIG. 15. Schematic model summarizing the radar and photogrammetric analyses at 2324:41 UTC. The relationship of the tornado with the hook echo, weak-echo column, lofted debris, and hydrometeors are illustrated. The debris overhang, hydrometeors encircling the weak-echo column, and debris pockets south of the tornado are shown. The updraft was inferred based on the debris overhang, weak-echo trench, and ρ_{hv} notch, and strong outbound velocities. The updraft is a branch of the much broader updraft that most likely includes much of the tornado. (a) Three-dimensional cross section and (b) vertical cross section.

strong outbound velocities. The updraft is a branch of the much broader updraft that most likely includes much of the tornado. Very small debris circulating within the WEC and dust/debris pockets located south of the tornado are both shown. Future work includes a detailed comparison of the polarimetric radar data with a comprehensive damage survey of the El Reno tornado.

Acknowledgments. Research results presented in the paper were supported the National Science Foundation by Grants RAPID AGS-1343963 and 1242339 (through NTA), AGS-1262048 and 0821231 (through HBB), and the Independent and Research/Development (IRD) program (through RMW). Some of the research was performed while one of the authors had a National Research Council Associateship Award at the National Severe Storms Laboratory. The authors wish to express their appreciation to Don Burgess and Tim Marshall for providing damage survey information that was integrated into the map shown in Fig. 1. The authors wish to thank Jim Marquis and two anonymous reviewers for providing helpful suggestions that improved an earlier version of the manuscript.

REFERENCES

Abrams, T., 1952: *The Manual of Photogrammetry*. George Banta Publishing, 876 pp.

Alexander, C. A., and J. Wurman, 2005: The 30 May 1998 Spencer, South Dakota, storm. Part I: The structural evolution and

environment of the tornadoes. *Mon. Wea. Rev.*, **133,** 72–97, doi:10.1175/MWR-2855.1.

Atkins, N. T., A. McGee, R. Ducharme, R. M. Wakimoto, and J. Wurman, 2012: The LaGrange tornado during VORTEX2. Part II: Photogrammetric analysis of the tornado combined with dual-Doppler radar data. *Mon. Wea. Rev.,* **140,** 2939–2958, doi:10.1175/MWR-D-11-00285.1.

——, K. M. Butler, K. R. Flynn, and R. M. Wakimoto, 2014: An integrated damage, visual, and radar analysis of the 2013 Moore, Oklahoma, EF5 tornado. *Bull. Amer. Meteor. Soc.,* **95,** 1549–1561, doi:10.1175/BAMS-D-14-00033.1.

Bluestein, H. B., J. G. LaDue, H. Stein, D. Speheger, and W. P. Unruh, 1993: Doppler radar wind spectra of supercell tornadoes. *Mon. Wea. Rev.,* **121,** 2200–2221, doi:10.1175/1520-0493(1993)121<2200:DRWSOS>2.0.CO;2.

——, W. P. Unruh, D. C. Dowell, T. A. Hutchinson, T. M. Crawford, A. C. Wood, and H. Stein, 1997: Doppler radar analysis of the Northfield, Texas, tornado of 25 May 1994. *Mon. Wea. Rev.,* **125,** 212–230, doi:10.1175/1520-0493(1997)125<0212:DRAOTN>2.0.CO;2.

——, B. A. Albrecht, R. M. Hardesty, W. D. Rust, D. Parsons, R. Wakimoto, and R. M. Rauber, 2001: Ground-based mobile instrument workshop summary, 23–24 February 2000, Boulder, Colorado. *Bull. Amer. Meteor. Soc.,* **82,** 681–694, doi:10.1175/1520-0477(2001)082<0681:MSGMIW>2.3.CO;2.

——, C. C. Weiss, and A. L. Pazmany, 2004: The vertical structure of a tornado near Happy, Texas, on 5 May 2002: High-resolution, mobile,W-band, Doppler radar observations. *Mon. Wea. Rev.,* **132,** 2325–2337, doi:10.1175/1520-0493(2004)132<2325:TVSOAT>2.0.CO;2.

——, ——, M. M. French, E. M. Holthaus, R. L. Tanamachi, S. Frasier, and A. L. Pazmany, 2007a: The structure of tornadoes near Attica, Kansas, on 12 May 2004: High-resolution, mobile, Doppler radar observations. *Mon. Wea. Rev.,* **135,** 475–506, doi:10.1175/MWR3295.1.

——, M. M. French, R. L. Tanamachi, S. Frazier, K. Hardwick, F. Junyent, and A. L. Pazmany, 2007b: Close-range observations of tornadoes in supercells made with a dual-polarization, X-band, mobile Doppler radar. *Mon. Wea. Rev.,* **135,** 1522–1543, doi:10.1175/MWR3349.1.

——, ——, I. PopStefanija, R. T. Bluth, and J. B. Knorr, 2010: A mobile, phased-array Doppler radar for the study of severe convective storms. *Bull. Amer. Meteor. Soc.,* **91,** 579–600, doi:10.1175/2009BAMS2914.1.

——, J. C. Snyder, and J. B. Houser, 2015: A multiscale overview of the El Reno, Oklahoma, tornadic supercell of 31 May 2013. *Wea. Forecasting,* in press.

Bodine, D. J., M. R. Kumjian, R. D. Palmer, P. L. Heinselman, and A. V. Ryzhkov, 2013: Tornado damage estimation using a polarimetric radar. *Wea. Forecasting,* **28,** 139–158, doi:10.1175/WAF-D-11-00158.1.

——, R. D. Palmer, and G. Zhang, 2014: Dual-wavelength polarimetric radar analyses of tornadic debris signatures. *J. Appl. Meteor. Climatol.,* **53,** 242–261, doi:10.1175/JAMC-D-13-0189.1.

Brown, R. A., L. R. Lemon, and D. W. Burgess, 1978: Tornado detection by pulsed Doppler radar. *Mon. Wea. Rev.,* **106,** 29–38, doi:10.1175/1520-0493(1978)106<0029:TDBPDR>2.0.CO;2.

Burgess, D., and Coauthors, 2014: 20 May 2013 Moore, Oklahoma, tornado: Damage survey and analysis. *Wea. Forecasting,* **29,** 1229–1237, doi:10.1175/WAF-D-14-00039.1.

Doswell, C. A., and D. W. Burgess, 1988: On some issues of United States tornado climatology. *Mon. Wea. Rev.,* **116,** 495–501, doi:10.1175/1520-0493(1988)116<0495:OSIOUS>2.0.CO;2.

——, H. E. Brooks, and N. Doztek, 2009: On the implementation of the enhanced Fujita scale in the USA. *Atmos. Res.,* **93,** 554–563, doi:10.1016/j.atmosres.2008.11.003.

Dowell, D. C., C. R. Alexander, J. M. Wurman, and L. J. Wicker, 2005: Centrifuging of hydrometeors and debris in tornadoes: Radar-reflectivity patterns and wind-measurement errors. *Mon. Wea. Rev.,* **133,** 1501–1524, doi:10.1175/MWR2934.1.

Fujita, T. T., 1981: Tornadoes and downbursts in the context of generalized planetary scales. *J. Atmos. Sci.,* **38,** 1511–1534, doi:10.1175/1520-0469(1981)038<1511:TADITC>2.0.CO;2.

——, G. S. Forbes, and T. A. Umenhofer, 1976: Close-up view of 20 March 1976 tornadoes: Sinking cloud tops to suction vortices. *Weatherwise,* **29,** 116–145, doi:10.1080/00431672.1976.10544142.

Hildebrand, P. H., and R. K. Moore, 1990: Meteorological radar observations from mobile platforms. *Radar in Meteorology,* D. Atlas, Ed., Amer. Meteor. Soc., 287–314.

Holle, R. L., 1986: Photogrammetry of thunderstorms. *Thunderstorms: A Social and Technological Documentary,* 2nd ed. E. Kessler, Ed., Vol. 3, University of Oklahoma, 77–98.

Isom, B., and Coauthors, 2013: The atmospheric imaging radar: Simultaneous volumetric observations using a phased array weather radar. *J. Atmos. Oceanic Technol.,* **30,** 655–675, doi:10.1175/JTECH-D-12-00063.1.

Koch, S. E., M. DesJardins, and P. J. Kocin, 1983: An interactive Barnes objective map analysis scheme for use with satellite and conventional data. *J. Climate Appl. Meteor.,* **22,** 1487–1503, doi:10.1175/1520-0450(1983)022<1487:AIBOMA>2.0.CO;2.

Kumjian, M. R., and A. V. Ryzhkov, 2008: Polarimetric signatures in supercell thunderstorms. *J. Appl. Meteor. Climatol.,* **47,** 1940–1961, doi:10.1175/2007JAMC1874.1.

Lee, W.-C., and J. Wurman, 2005: Diagnosed three-dimensional axisymmetric structure of the Mulhall tornado on 3 May 1999. *J. Atmos. Sci.,* **62,** 2373–2393, doi:10.1175/JAS3489.1.

Lemon, L. R., and C. A. Doswell, 1979: Severe thunderstorm evolution and mesocyclone structure as related to tornadogenesis. *Mon. Wea. Rev.,* **107,** 1184–1197, doi:10.1175/1520-0493(1979)107<1184:STEAMS>2.0.CO;2.

Lewellen, D. C., B. Gong, and W. S. Lewellen, 2008: Effects of finescale debris on near-surface tornado dynamics. *J. Atmos. Sci.,* **65,** 3247–3262, doi:10.1175/2008JAS2686.1.

Malkus, J., 1952: The slopes of cumulus clouds in relation to external wind shear. *Quart. J. Roy. Meteor. Soc.,* **78,** 530–542, doi:10.1002/qj.49707833804.

Palmer, R. D., and Coauthors, 2011: Observations of the 10 May 2010 tornado outbreak using OU-PRIME: Potential for new science with high-resolution polarimetric radar. *Bull. Amer. Meteor. Soc.,* **92,** 871–891, doi:10.1175/2011BAMS3125.1.

Pazmany, A. L., J. B. Mead, H. B. Bluestein, J. C. Snyder, and J. B. Houser, 2013: A mobile rapid-scanning X-band polarimetric (RaXPol) Doppler radar system. *J. Atmos. Oceanic Technol.,* **30,** 1398–1413, doi:10.1175/JTECH-D-12-00166.1.

Rasmussen, E. N., and J. M. Straka, 2007: Evolution of low-level angular momentum in the 2 June 1995 Dimmitt, Texas, tornado cyclone. *J. Atmos. Sci.,* **64,** 1365–1378, doi:10.1175/JAS3829.1.

Ryzhkov, A. V., T. J. Schur, D. W. Burgess, and D. S. Zrnic, 2005a: Polarimetric tornado detection. *J. Appl. Meteor.,* **44,** 557–570, doi:10.1175/JAM2235.1.

——, ——, ——, P. L. Heinselman, S. E. Grangrande, and D. S. Zrnic, 2005b: The joint polarization experiment: Polarimetric

rainfall measurements and hydrometeor classification. *Bull. Amer. Meteor. Soc.,* **86,** 809–824, doi:10.1175/BAMS-86-6-809.

Snyder, J. C., and H. B. Bluestein, 2014: Some considerations for the use of high-resolution mobile radar data in tornado intensity. *Wea. Forecasting,* **29,** 799–827, doi:10.1175/WAF-D-14-00026.1.

Tanamachi, R. L., H. B. Bluestein, J. B. Houser, S. J. Frasier, and K. M. Hardwick, 2012: Mobile, X-band, polarimetric Doppler radar observations of the 4 May 2007 Greensburg, Kansas, tornadic supercell. *Mon. Wea. Rev.,* **140,** 2103–2125, doi:10.1175/MWR-D-11-00142.1.

Van Den Broeke, M. S., J. M. Straka, and E. N. Rasmussen, 2008: Polarimetric radar observations at low levels during tornado life cycles in a small sample of classic southern plains supercells. *J. Appl. Meteor. Climatol.,* **47,** 1232–1247, doi:10.1175/2007JAMC1714.1.

Vivekanandan, J., D. S. Zrnic, S. M. Ellis, R. Oye, A. V. Ryzhkov, and J. Straka, 1999: Cloud microphysics retrieval using S-band dual-polarization radar measurements. *Bull. Amer. Meteor. Soc.,* **80,** 381–388, doi:10.1175/1520-0477(1999)080<0381:CMRUSB>2.0.CO;2.

Wakimoto, R. M., and B. E. Martner, 1992: Observations of a Colorado tornado. Part II: Combined photogrammetric and Doppler radar analysis. *Mon. Wea. Rev.,* **120,** 522–543, doi:10.1175/1520-0493(1992)120<0522:OOACTP>2.0.CO;2.

——, W.-C. Lee, H. B. Bluestein, C.-H. Liu, and P. H. Hildebrand, 1996: ELDORA observations during VORTEX 95. *Bull. Amer. Meteor. Soc.,* **77,** 1465–1481, doi:10.1175/1520-0477(1996)077<1465:EODV>2.0.CO;2.

——, H. V. Murphey, D. C. Dowell, and H. B. Bluestein, 2003: The Kellerville tornado during VORTEX: Damage survey and Doppler radar analyses. *Mon. Wea. Rev.,* **131,** 2197–2221, doi:10.1175/1520-0493(2003)131<2197:TKTDVD>2.0.CO;2.

——, N. T. Atkins, and J. Wurman, 2011: The LaGrange tornado during VORTEX2. Part I: Photogrammetric analysis of the tornado combined with single-Doppler radar data. *Mon. Wea. Rev.,* **139,** 2233–2258, doi:10.1175/2010MWR3568.1.

——, P. Stauffer, W.-C. Lee, N. T. Atkins, and J. Wurman, 2012: Finescale structure of the LaGrange, Wyoming, tornado during VORTEX2: GBVTD and photogrammetric analyses. *Mon. Wea. Rev.,* **140,** 3397–3418, doi:10.1175/MWR-D-12-00036.1.

Wurman, J., 2002: The multiple-vortex structure of a tornado. *Wea. Forecasting,* **17,** 473–505, doi:10.1175/1520-0434(2002)017<0473:TMVSOA>2.0.CO;2.

——, and S. Gill, 2000: Finescale radar observations of the Dimmitt, Texas (2 June 1995), tornado. *Mon. Wea. Rev.,* **128,** 2135–2164, doi:10.1175/1520-0493(2000)128<2135:FROOTD>2.0.CO;2.

——, and M. Randall, 2001: An inexpensive, mobile, rapid-scan radar. Preprints, *30th Int. Conf on Radar Meteorology,* Munich, Germany, Amer. Meteor. Soc., P3.4. [Available online at https://ams.confex.com/ams/30radar/techprogram/paper_21577.htm.]

——, and K. Kosiba, 2013: Finescale radar observations of tornado and mesocyclone structures. *Wea. Forecasting,* **28,** 1157–1174, doi:10.1175/WAF-D-12-00127.1.

——, J. M. Straka, and E. N. Rasmussen, 1996: Fine-scale Doppler radar observations of tornadoes. *Science,* **272,** 1774–1777, doi:10.1126/science.272.5269.1774.

——, Y. Richardson, C. Alexander, S. Weygandt, and P. F. Zhang, 2007a: Dual-Doppler and single-Doppler analysis of a tornadic storm undergoing mergers and repeated tornadogenesis. *Mon. Wea. Rev.,* **135,** 736–758, doi:10.1175/MWR3276.1.

——, ——, ——, ——, and ——, 2007b: Dual-Doppler analysis of winds and vorticity budget terms near a tornado. *Mon. Wea. Rev.,* **135,** 2392–2405, doi:10.1175/MWR3404.1.

——, K. Kosiba, P. Robinson, and T. Marshall, 2014: The role of multiple-vortex tornado structure in causing storm researcher fatalities. *Bull. Amer. Meteor. Soc.,* **95,** 31–45, doi:10.1175/BAMS-D-13-00221.1.

Zehnder, J. A., J. Hu, and A. Razdan, 2007: A stereo photogrammetric technique applied to orographic convection. *Mon. Wea. Rev.,* **135,** 2265–2277, doi:10.1175/MWR3401.1.

Zrnic, D. S., and A. V. Ryzhkov, 1998: Observations of insects and birds with a polarimetric radar. *IEEE Trans. Geosci. Remote Sens.,* **36,** 661–668, doi:10.1109/36.662746.

——, and ——, 1999: Polarimetry for weather surveillance radars. *Bull. Amer. Meteor. Soc.,* **80,** 389–406, doi:10.1175/1520-0477(1999)080<0389:PFWSR>2.0.CO;2.